

# Tornadogenesis in a High-Resolution Simulation of the 8 May 2003 Oklahoma City Supercell

ALEXANDER D. SCHENKMAN

*Center for Analysis and Prediction of Storms, University of Oklahoma, Norman, Oklahoma*

MING XUE

*Center for Analysis and Prediction of Storms, and School of Meteorology, University of Oklahoma, Norman, Oklahoma*

MING HU

*Cooperative Institute for Research in Environmental Sciences, University of Colorado, Boulder, Colorado*

(Manuscript received 25 February 2013, in final form 14 August 2013)

## ABSTRACT

A 50-m-grid-spacing Advanced Regional Prediction System (ARPS) simulation of the 8 May 2003 Oklahoma City tornadic supercell is examined. A 40-min forecast run on the 50-m grid produces two F3-intensity tornadoes that track within 10 km of the location of the observed long-track F4-intensity tornado.

The development of both simulated tornadoes is analyzed to determine the processes responsible for tornadogenesis. Trajectory-based analyses of vorticity components and their time evolution reveal that tilting of low-level frictionally generated horizontal vorticity plays a dominant role in the development of vertical vorticity near the ground. This result represents the first time that such a mechanism has been shown to be important for generating near-surface vertical vorticity leading to tornadogenesis.

A sensitivity simulation run with surface drag turned off was found to be considerably different from the simulation with drag included. A tornado still developed in the no-drag simulation, but it was much shorter lived and took a substantially different track than the observed tornadoes as well as the simulated tornadoes in the drag simulation. Tilting of baroclinic vorticity in an outflow surge may have played a role in tornadogenesis in the no-drag simulation.

## 1. Introduction

It has been over 50 years since Browning (1962) introduced the term “supercell” to describe single large thunderstorm cells with rotating updrafts. In the intervening years, research on supercells and tornadoes has yielded tremendous progress in our understanding of the dynamical processes and environmental conditions associated with these meteorological phenomena. Yet, despite large leaps in knowledge, a complete understanding of tornado formation and evolution remains elusive (Wurman et al. 2012).

The basis for much of the current understanding of supercell dynamics originated with the pioneering

numerical and theoretical studies performed in the late 1970s and first half of the 1980s (Klemp and Wilhelmson 1978a,b; Schlesinger 1978; Wilhelmson and Klemp 1978; Schlesinger 1980; Klemp et al. 1981; Klemp and Rotunno 1983; Davies-Jones 1984; Rotunno and Klemp 1985). These studies provided explanations of many observed features of supercells including storm splitting, midlevel rotation, occlusion downdrafts, and to some extent, low-level rotation, which developed as parcels descended within the forward-flank baroclinic zone (Klemp and Rotunno 1983; Rotunno and Klemp 1985). The development of vertical vorticity in this manner was later explained by Davies-Jones and Brooks (1993) as being the result of “slippage” between vortex lines and trajectories due to horizontal baroclinic streamwise vorticity generation during parcel descent.

Capitalizing on improved computational capabilities, Wicker and Wilhelmson (1995, hereafter WW95) performed a similar study to Klemp and Rotunno (1983),

---

*Corresponding author address:* Alexander D. Schenkman, Center for Analysis and Prediction of Storms, University of Oklahoma, 120 David L. Boren Blvd., Norman, OK 73072.  
E-mail: alex3238@ou.edu

except with much higher spatial resolution [with a minimum vertical (horizontal) spacing of 50 (120) m as opposed to 500 (250) m in Klemp and Rotunno (1983)]. The simulation in WW95 produced two tornado-strength vortices, both of which were preceded by intensification of the lower- to midlevel mesocyclone. According to their interpretation, the increased rotation in the mesocyclone led to upward pressure gradient forces that were responsible for generating a strong low-level updraft. In turn, this low-level updraft tilted baroclinically generated horizontal vorticity into the vertical and then stretched it leading to tornadogenesis. WW95 was unable to explain the development of rotation next to the surface and they did not discuss the cause of the midlevel mesocyclone intensification responsible for low-level updraft intensification.

Most of the explanations provided by the numerical studies of the 1980s and 1990s have been confirmed (or at least not disproven) observationally over the past few decades. However, the relationship between storm-generated baroclinity and tornadoes (as well as between the low-level mesocyclone and tornado) has been drawn into question by the observations obtained during the Verification of the Origin of Rotation in Tornadoes Experiment (VORTEX; Rasmussen et al. 1994). Specifically, Markowski et al. (2002) found that rear-flank downdrafts (RFDs) in tornadic supercells were significantly warmer than RFDs in their nontornadic counterparts. This result was confirmed in Grzych et al. (2007), and warm RFDs in tornadic supercells have also been found by Hirth et al. (2008) and Lee et al. (2011, 2012). Shabbot and Markowski (2006) performed a similar study to Markowski et al. (2002) for the forward-flank downdraft (FFD) region in supercells intercepted by VORTEX and found a similar result—namely, that tornadic FFDs were warmer than nontornadic FFDs. Meanwhile, observations from VORTEX also showed a surprising lack of distinguishable differences in the kinematic fields of tornadic and nontornadic supercells. Trapp (1999) presented observations from six supercells, three of which were tornadic. These observations showed that both the tornadic and nontornadic storms contained persistent low-level mesocyclones, suggesting that the physical mechanisms explaining the genesis of low-level mesocyclones may not be sufficient to explain tornadogenesis. In agreement with Trapp (1999), Wakimoto and Cai (2000) compared observations from a tornadic and nontornadic supercell and found very similar structures for the two storms, with virtually identical low-level mesocyclones. Wakimoto and Cai (2000) found that the only differences between the two storms were stronger updrafts along the rear-flank gust front (RFGF), stronger storm-relative inflow, and more

precipitation behind the RFGF for the nontornadic storm. Markowski et al. (2011) also found very similar kinematic fields in tornadic and nontornadic supercells.

Using vortex line analyses (Straka et al. 2007), more recent studies (Markowski et al. 2008, 2011, 2012a,b; Marquis et al. 2012) have suggested that horizontal vorticity is “arched” over the RFD and/or supercell hook echo to create a vortex couplet. The vortex line making up these arches has a much different orientation than the environmental vorticity and, instead, is oriented in a manner much more consistent with baroclinically generated vorticity. Unfortunately, these observational studies<sup>1</sup> generally do not have high-enough spatiotemporal resolution to directly analyze the kinematic and especially thermodynamic fields associated with tornado-scale features. As such, any specific link between these findings and the genesis/intensification of tornado-scale vortices necessarily contains a degree of speculation.

Taken as a whole, the results of these observational studies suggest that the relationship between baroclinity and tornadogenesis may be subtle. Markowski and Richardson (2009) suggest that tornadogenesis may be a Goldilocks phenomenon whereby the downdraft-induced thunderstorm outflow or cold pool cannot be too warm (i.e., baroclinity has to be present) or too cold (i.e., not so cold that it undercuts the storm or prevents near-surface parcels from being dynamically lifted), but “just right” (baroclinity generates horizontal vorticity, which is reoriented into the vertical and then significantly amplified by stretching). The idealized modeling study of Snook and Xue (2008) also suggests that the cold pool intensity that is sensitive to model microphysics needs to be just about right to support tornadogenesis but it was the vertical alignment of the mid- to low-level mesocyclone and low-level rotation that they emphasized to be important in their study. Given that a low-level mesocyclone seems to be a necessary, but not sufficient condition for tornadogenesis (Trapp et al. 2005), an alternative interpretation of the above results is that the mechanisms responsible for generating the mesocyclone may differ from those responsible for tornadogenesis.

Although many valuable insights on supercell dynamics have been gained through the idealized modeling studies of the 1980s and 1990s, such idealized simulations typically neglect factors such as environmental heterogeneity and surface processes that may be important to tornadogenesis. Studies based on

---

<sup>1</sup> Data assimilation is performed in addition to the dual-Doppler analysis in Marquis et al. (2012). However, the model grid spacing is 500 m, which is not sufficient to resolve the tornadic scale.

numerical simulations of sufficiently high resolution of real tornadic thunderstorms are few in the published literature. In this study, we perform dynamic analyses on tornadogenesis processes in a “classic” tornadic supercell simulated with nested grids with as small as 50-m horizontal grid spacing. This simulation includes a full physics model that parameterizes surface processes and starts from a realistic initial condition obtained through assimilation of Doppler radar and other high-resolution observations. To our knowledge, this study is the first to examine tornadogenesis in a “classic” tornadic supercell simulated with fine-enough grid spacing to explicitly resolve a tornado-like vortex while also including surface effects and environmental heterogeneity. In fact, as far as we know, this study is only the third to investigate a tornadic storm with realistic experiment design and methodology. The other two studies, Mashiko et al. (2009) and Schenkman et al. (2012), examined tornadogenesis in a minisupercell within a typhoon rainband and in a quasi-linear convective system (QLCS), respectively.

Mashiko et al. (2009) found that secondary RFD surges were critical to tornadogenesis in their high-resolution simulations of a minisupercell associated with a land-falling typhoon. They explain that, in addition to enhancing convergence, the secondary RFD surges provide an additional source of vorticity by transporting large streamwise vorticity, associated with the extreme low-level shear in the typhoon environment, into the inflow of the developing tornado. By conducting sensitivity experiments in which they turned off water loading or evaporation, they concluded that the secondary RFD surges in their simulation were the result of water loading. A tornado did not form in experiments when water loading was turned off.

While the results presented in Mashiko et al. (2009) are compelling for the tropical minisupercell they considered, it is unknown how applicable the study is to the more typical supercell environment, which tends to have a much drier boundary layer with comparatively less low-level environmental helicity. Mashiko et al. (2009) also found frictional generation of horizontal vorticity is relatively small and unimportant in tornadogenesis in their simulation. However, their simulation was conducted for a storm that was predominantly located over water where friction is much smaller compared to that over land.

In contrast, Schenkman et al. (2012) found a very substantial impact of surface drag on tornadogenesis in a QLCS mesovortex tornadogenesis case they examined. Specifically, an adverse pressure gradient force associated with the gust front in their simulation led to boundary layer separation of the frictional layer and the subsequent development of a strong horizontal rotor.

The upward branch of this rotor was found to be responsible for a strong low-level updraft that concentrated and stretched mesovortex vorticity to tornadic intensity. When drag was turned off in their simulation, they found that the horizontal rotor and associated low-level updraft were absent, leading to the failure of tornado-like vortex formation.

The present study examines a tornadic supercell that occurred near Oklahoma City (OKC) on 8 May 2003 using a similar methodology to that of Schenkman et al. (2012). In particular, it seeks to determine the origin of vorticity for the simulated tornadoes in the simulated OKC tornadic supercell. In a recent review of tornado dynamics, Rotunno (2013) concludes “It is the present author’s opinion that further progress awaits a deeper understanding of the connection between laboratory flows, for which boundary layer effects are critically important and effects of cool boundaries are absent, and studies of natural mesocyclones, for which boundary layer effects are typically given secondary consideration (and are very difficult to observe) to the effects of cool-air boundaries.” Our study seeks to begin to make such a connection.

The remainder of this paper is organized as follows: Section 2 presents a brief description of the 8 May 2003 OKC tornadic supercell. Experiment methodology and design are discussed in section 3. Section 4 begins with an overview of the simulation and then proceeds to analyze tornadogenesis. A free-slip lower-boundary sensitivity study is also presented in section 4. Conclusions and future directions are discussed in section 5.

## 2. Case overview

The 8 May 2003 Oklahoma City supercell (OKC supercell) formed in the middle of an unusually long tornado outbreak that occurred over much of the central United States from 3 to 11 May 2003, producing 361 tornadoes (Hamill et al. 2005). Hamill et al. (2005) studied this extended outbreak and found that it was the result of a persistent large-scale trough over the southwestern United States. Intermittent shortwave troughs moving through the longwave trough led to daily tornado outbreaks from the central and southern plains into the mid-Atlantic region. A notable aspect of the extended outbreak was the lack of any strong cold fronts within the affected area, meaning that warm, moist air from the gulf was continually present, leading to copious instability for tornadic supercells when combined with the deep-layer wind shear associated with shortwave troughs moving through the persistent longwave trough.

The OKC supercell was initiated along a dryline in central Oklahoma around 2100 UTC 8 May 2003. The

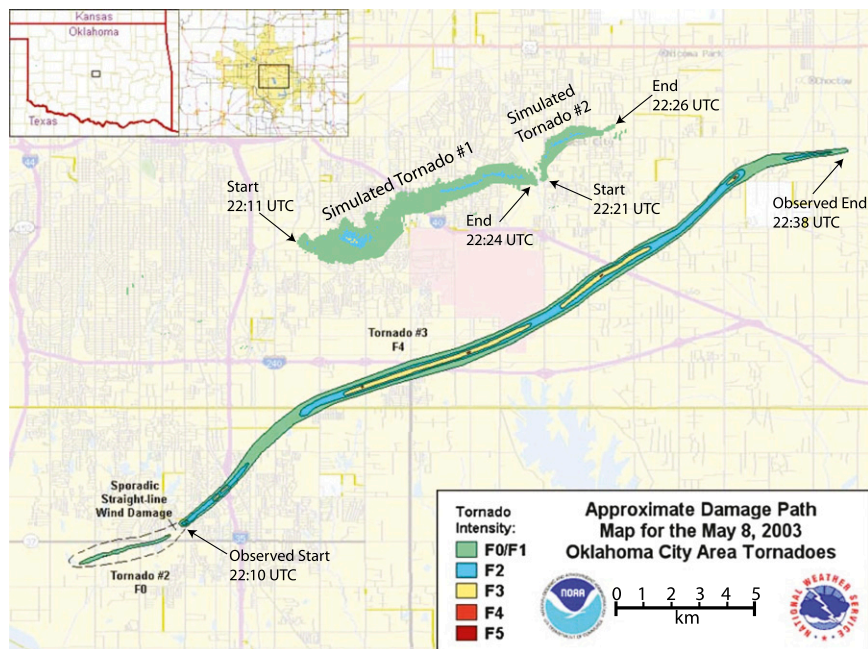


FIG. 1. Map of the southern Oklahoma City area overlaid with the track of the simulated tornadoes and the observed tornadoes on 8 May 2003. Image is adapted from the Norman, OK, National Weather Service (NWS) website: <http://www.srh.noaa.gov/oun/?n=events-20030508>.

storm formed in an environment with large mixed-layer CAPE ( $>3800 \text{ J kg}^{-1}$ ) and storm-relative environmental helicity (SREH) of greater than  $450 \text{ m}^2 \text{ s}^{-2}$  [see Fig. 3 in Romine et al. (2008)]. The storm rapidly took on supercell characteristics and produced two weak, short-lived tornadoes just southwest of Moore, Oklahoma, between 2200 and 2208 UTC. At 2210 UTC, a third tornado formed on the western side of Moore and persisted for 28 min, producing widespread F2–F3 and localized F4 damage along its roughly 27-km track (Fig. 1). Following the dissipation of this tornado, the OKC supercell began to weaken with no additional tornadoes. The OKC supercell dissipated shortly after 0000 UTC 9 May 2003.

Owing to its proximity to a major metropolitan area and the high observation density present in Oklahoma, varying aspects of the OKC supercell have been examined and discussed in several past studies (Ryzhkov et al. 2005; Hu and Xue 2007; Liu et al. 2007; Romine et al. 2008; Dowell and Wicker 2009; Kumjian and Ryzhkov 2009; Dowell et al. 2011; Gao and Stensrud 2012). For the most part, these studies use data from the OKC supercell as a test or demonstration case for a variety of topics including polarimetric radar data analysis (e.g., Ryzhkov et al. 2005; Romine et al. 2008; Kumjian and Ryzhkov 2009), data assimilation techniques (e.g., Dowell and Wicker 2009; Dowell et al. 2011; Gao and Stensrud 2012), tornado detection/characterization algorithms (Liu

et al. 2007; Wang et al. 2008; Potvin et al. 2009), and advection correction techniques (Shapiro et al. 2010).

Using polarimetric radar observations, Romine et al. (2008) performed the most detailed dynamical analysis of the OKC supercell. However, their study was mainly focused on the behavior of the polarimetric variables and possible microphysical implications. One notable aspect of Romine et al. (2008) was the observation that the FFGF was associated with meager temperature perturbations with much larger cold perturbations behind the RFGF. On the other hand, Romine et al. (2008) reaches this conclusion primarily based on data from only two stationary surface observation sites, which likely means that thermodynamic structure of the cold pool was largely unresolved.

### 3. Simulation experiment methodology

The simulation of the 8 May 2003 OKC tornadic supercell is performed using the Advanced Regional Prediction System (ARPS; Xue et al. 1995, 2000, 2001, 2003) model using four one-way nested grids in order to capture the evolution of the 8 May 2003 tornado outbreak on a variety of scales (Fig. 2). The outermost grid has 9-km grid spacing, covers a  $2300 \text{ km} \times 2300 \text{ km}$  area, and assimilates hourly conventional data (including Oklahoma Mesonet data) using the ARPS three-dimensional variational data assimilation (3DVAR)

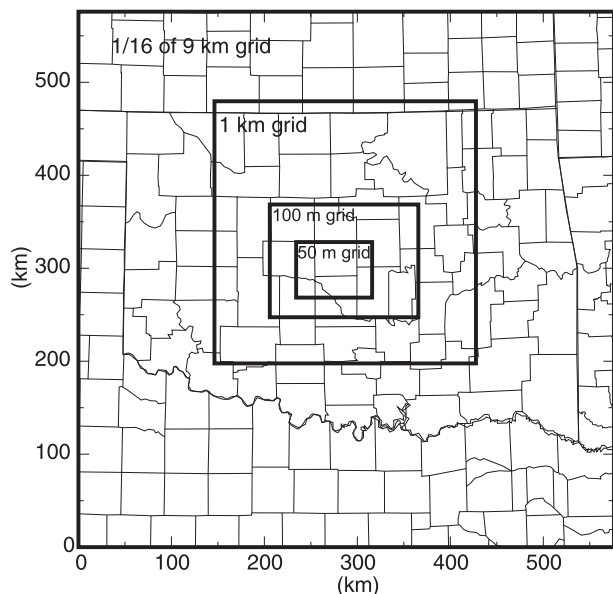


FIG. 2. Map of  $1/16$  of 9-km-grid-spacing simulation domain with black rectangles marking the boundaries of 1-km-, 100-m-, and 50-m-grid-spacing domains.

(Gao et al. 2004; Hu et al. 2006a,b) between 1800 UTC 8 May and 0000 UTC 9 May 2003. Rawinsonde data are also assimilated at 1800 and 0000 UTC. The 1800 UTC National Centers for Environmental Prediction (NCEP) operational Eta model analysis is used to provide initial analysis background at 1800 UTC and the boundary conditions come from the Eta forecasts every 3 h. The 9-km forecast used here is the same as that reported in Hu and Xue (2007), which focused on the impact of radar data assimilation cycles on a nested 3-km grid. In this study, a 1-km instead of a 3-km-grid-spacing domain is nested within the 9-km domain. This 1-km-grid-spacing domain covers a  $280 \text{ km} \times 280 \text{ km}$  area. On this 1-km grid, 5-min data assimilation cycles are performed over a 70-min period beginning at 2030 UTC 8 May 2003. Radial velocity data from the Weather Surveillance Radar-1988 Doppler (WSR-88D) at Twin Lakes (KTLX) Oklahoma City are assimilated within these cycles via the ARPS 3DVAR while the reflectivity data are assimilated using a complex cloud analysis package (Hu et al. 2006a). More details on the data assimilation configurations and verification of the general behaviors of the forecasts can be found in Xue et al. (2013).

Two very-high-resolution domains are nested within the 1-km domain. The first has 100-m grid spacing, covers a  $160 \text{ km} \times 120 \text{ km}$  area, and begins a 60-min forecast at 2140 UTC, obtaining its initial condition from the 1-km final analysis and its boundary conditions from the 1-km forecast at 1-min intervals. A 50-m-grid-spacing domain that covers an  $80 \text{ km} \times 60 \text{ km}$  area is further

nested within the 100-m simulation; its 40-min-long simulation starts from the interpolated 100-m forecast at 2200 UTC. No additional data assimilation is performed on the 100- or 50-m grid. All four model domains use a stretched vertical coordinate with 53 vertical levels and a minimum grid spacing of 20 m near the model ground. The lowest vector and scalar model grid point is about 10 m AGL.

Model configurations for the 100- and 50-m-grid-spacing simulations include Lin 3 ice microphysics with the rain intercept parameter set at the default value of  $8 \times 10^6 \text{ m}^{-4}$ , fourth-order advection in the horizontal and vertical, a rigid top boundary condition with a wave-absorbing layer beginning at 12 km AGL, fourth-order computational mixing, a 1.5-order TKE-based subgrid-scale turbulent mixing scheme, and PBL parameterization. Surface fluxes are calculated using stability-dependent drag coefficients (Byun 1990) while surface roughness length is dependent on the vegetation properties. The Coriolis parameter includes the effect of earth curvature. A two-layer soil model is used that is based on Noilhan and Planton (1989). Radiative processes are calculated from the National Aeronautics and Space Administration (NASA) Goddard Space Flight Center long- and shortwave radiation package. More details on the physics options within the ARPS can be found in Xue et al. (2001, 2003). Because the focus of the present study is on the dynamical processes responsible for tornadogenesis in the OKC storm, the remainder of this paper is focused on the 50-m-grid-spacing simulation. We note here that the simulation of tornado vortices on the 100-m grid spacing is generally similar to those of simulation of the 50-m grid. The 100-m simulation was launched about 30 min before the simulated tornado within the model while the 50-m grid is further one-way nested inside 20 min later. The consistency between the 100- and 50-m simulations suggests that the simulated tornado is not an artifact of model spinup. Additional details on the simulation and verification can be found in Xue et al. (2013).

#### 4. Simulation results and tornadogenesis processes

In this section, the general evolution of the simulated 8 May 2003 OKC supercell storm is first discussed. We then provide an overview of the evolution of low-level features that are considered important for tornadogenesis processes. This discussion is followed by a more detailed analysis of the dynamics responsible for tornadogenesis in this simulation. In this study, a simulated vortex is considered a tornado if it has winds greater than  $32 \text{ m s}^{-1}$  (F1 intensity) at the first grid level (about 10 m) above the surface, a core radius of about 1 km or less, and if it persists for more than 2 min.

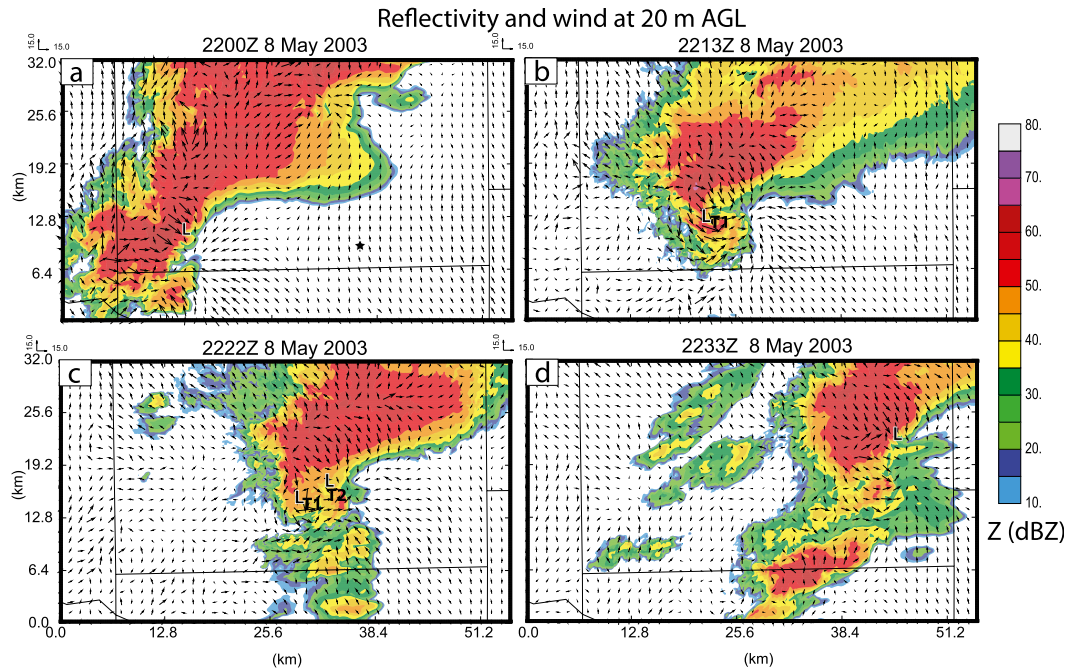


FIG. 3. Simulated reflectivity (dBZ) and low-level wind vectors ( $\text{m s}^{-1}$ ) 20 m AGL at (a) 2200, (b) 2213, (c) 2222, and (d) 2233 UTC from the 50-m-grid-spacing simulation of 8 May 2003 OKC tornadic supercell. The location of the low-level mesocyclone at 1 km AGL is marked by “L.” “T1” and “T2” mark the locations of tornadoes 1 and 2, respectively. The star in (a) marks the location of an extracted wind profile plotted in Fig. 4.

#### a. Storm-scale overview of the simulation

The 50-m simulation begins at 2200 UTC with a developing supercell in the western half of the model domain (Fig. 3a). A low-level mesocyclone<sup>2</sup> is present along the leading edge of the southern portion of high reflectivity in the storm. At midlevels, a broad mesocyclone and updraft of greater than  $50 \text{ m s}^{-1}$  is present (not shown). As is expected in a supercell storm, this mid-level updraft and mesocyclone persist (with occasional pulses in intensity) throughout the model simulation (not shown). Large low-level shear is present in the inflow to the supercell, with particularly large shear in the lowest 100 m of the simulation owing to the effects of the surface drag that is included in the simulation (Fig. 4). It should be noted that Chow et al. (2005) found that standard eddy viscosity models, such as the 1.5-order TKE-based scheme used herein, led to overestimation of the frictionally generated low-level shear in their model. However, the qualitative impact of surface drag

on the low-level flow should be the same even if it is overestimated.

By 2213 UTC, the supercell has taken on a “classic” appearance with a strong tornado (tornado 1) located at the tip of a well-defined hook-echo structure (Fig. 3b). The tornado is located on the southeastern side of a low-level mesocyclone. Over the next 10 min, the supercell undergoes an occlusion cycle and a new tornado (tornado 2) and low-level mesocyclone develop about 5 km to the east of tornado 1 (Fig. 3c). By 2233 UTC (Fig. 3d), both tornadoes have dissipated and, although a low-level mesocyclone is still apparent at 1 km AGL, the supercell has started to become dominated by cold outflow (not shown) and has weakened. The supercell weakens steadily throughout the remainder of the simulation.

#### b. Tornado-scale overview of the simulation

Having provided a general overview of the simulated OKC supercell, we turn our attention to the evolution of the low-level kinematic and thermodynamic fields, focusing on aspects most related to the simulated tornadoes. At 2200 UTC, a large cold pool occupies the western portion of the model domain, as indicated by the surface potential temperature ( $\theta$ ) field (Fig. 5a). The leading edge of the southern portion of the cold pool (or gust front) is oriented from south-southwest to north-northeast. Farther north, the cold pool extends to the

<sup>2</sup>Though we mark low-level mesocyclones in Fig. 3, their definition is somewhat subjective as smaller-scale features dominate, making objective criteria based on, for example, vertical vorticity, difficult to apply. Instead, low-level mesocyclones are identified by subjectively locating the center of mesoscale rotation at 1 km AGL.

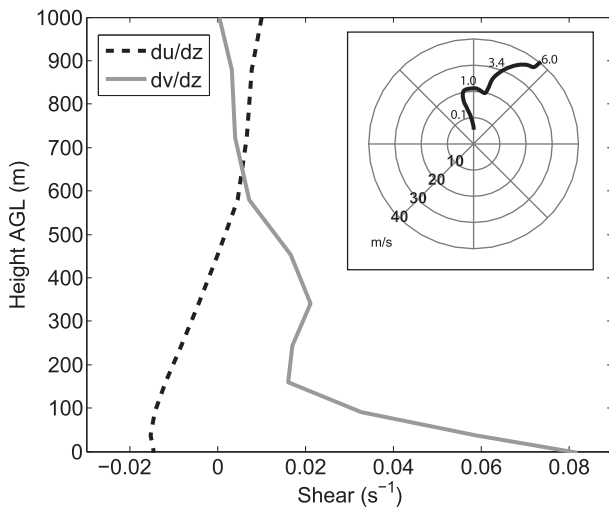


FIG. 4. Low-level vertical shear profile from an extracted sounding located at the black star in Fig. 3 at 2200 UTC. The inset shows the 0–6-km hodograph from the same location.

east-northeast with a less well-defined  $\theta$  gradient (dotted line in Fig. 5a). The makeup of the southern portion of the cold pool is initially very heterogeneous, with several pockets of high- and low- $\theta$  air and a secondary gust front marking an area of much stronger westerly flow about 5 km to the west of the main gust front (thin solid black line in Fig. 5a). With time, the cold pool becomes more organized and homogeneous with the development of a well-defined RFGF by 2206 UTC (Fig. 5b). To the northeast of the RFGF, a forward-flank convergence

boundary (FFCB; Beck and Weiss 2013) marks the interface between the storm inflow and rain-cooled air in the forward flank of the supercell. To the northwest of the RFGF, an internal RFD surge has formed and is moving to the southeast; the leading edge of this RFD surge is indicated by the thin solid black line in Fig. 5b.

The internal RFD surge behind the RFGF is associated with several small vorticity maxima at the time of Fig. 5b. None of these maxima organize into a tornado-strength vortex and the internal surge gradually becomes less defined, blending in with the cold pool behind the RFGF (not shown). Over the next couple of minutes, two small, shallow, near-surface vertical vorticity maxima form in the vicinity of the RFGF. The first vorticity maximum (V1) forms around 2207:30 UTC (Fig. 6a) and intensifies while moving northeast, north, and finally slightly to the west (Figs. 6b,c). V1 is strongest (in terms of vertical vorticity) at the lowest model level and weakens with height, becoming difficult to identify above 500 m AGL. The second vorticity maximum (V2) first becomes apparent near the surface at around 2208 UTC (Fig. 6b) to the north of V1 and remains nearly stationary. V2 is also confined to the lowest roughly 500 m of the simulation; however, unlike V1, V2 is most intense about 200 m AGL. As V1 moves to the north and west it intensifies and absorbs V2 to create a pretornadic vortex (PTV) around 2209:30 UTC (Figs. 6c,d). The PTV is fairly intense (in terms of maximum vorticity values), but is only about 800 m deep and is compact with winds weaker than tornado strength.

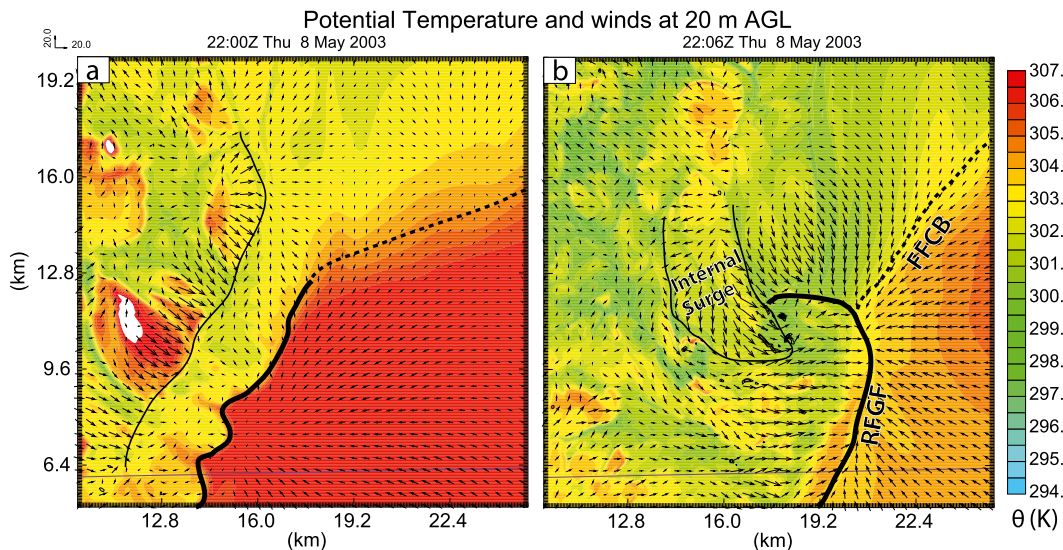


FIG. 5. Potential temperature (shaded, K) and horizontal wind vectors ( $\text{m s}^{-1}$ ) at 20 m AGL of the 50-m-simulation domain (the  $x$  and  $y$  axes have their origin at the lower-left corner of the domain) at (a) 2200 and (b) 2206 UTC 8 May 2003. In (b) the locations of the RFGF (solid black line), FFCB (dashed black line), and an internal outflow surge (indicated by the solid thin line at the leading edge) are marked.

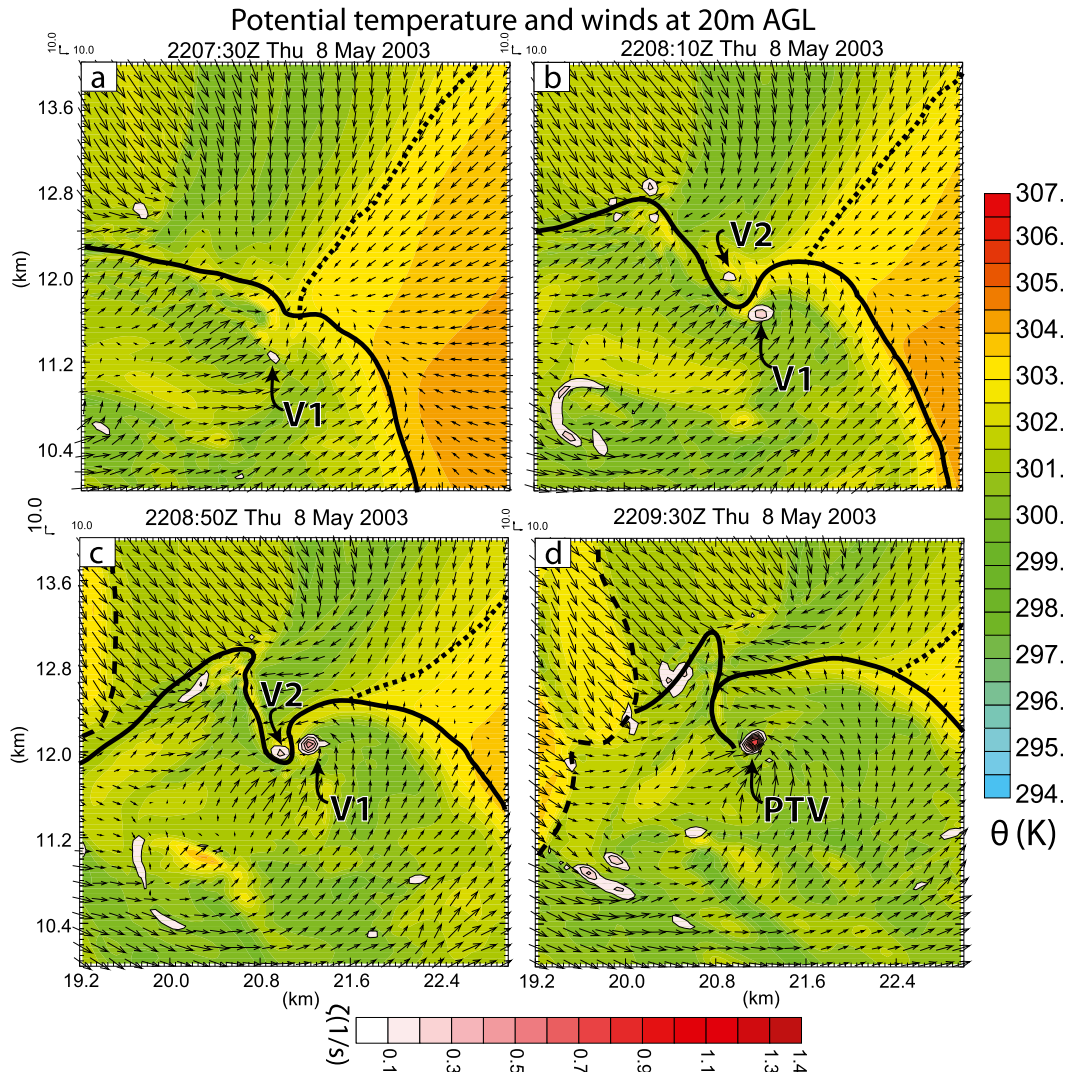


FIG. 6. Potential temperature (shaded, K), horizontal wind vectors ( $\text{m s}^{-1}$ ), and vertical vorticity (black contours filled with red hue shading, starting at  $0.1 \text{ s}^{-1}$ ) at 20 m AGL at (a) 2207:30, (b) 2208:10, (c) 2208:50, and (d) 2209:30 UTC 8 May 2003. Gust fronts are denoted with the same convention as Fig. 5. In (c),(d) the long dashed line marks the leading edge of an internal outflow surge.

Concurrent with the development of the PTV, an internal RFD surge begins to overtake the RFGF (Figs. 6c,d). This internal RFD surge originated at about 2206 UTC about 5 km northwest of the PTV and is a different surge from the one shown in Fig. 5b. The air behind the internal RFD surge is relatively warm (Fig. 6d), associated with a simulated reflectivity maximum (not shown), and backward trajectory analysis suggests that this surge is composed of air that originated a few kilometers above the surface that is not saturated as it descends (not shown). All of this suggests that the internal RFD surge is the result of a downdraft that was caused primarily by water loading in the core of the OKC supercell. With time, the internal surge cools (Fig. 7) owing to continued

evaporation in the heavy precipitation. The internal surge rapidly moves to the southeast and approaches the PTV around 2210 UTC (Fig. 7a). A few small vorticity maxima are present along the leading edge of the internal surge, with one maximum in particular (V3) appearing to merge with the PTV (Figs. 7b,c). As V3 merges with the PTV, tornadogenesis occurs rapidly around 2211 UTC (Fig. 7d). The simulated tornado (tornado 1) moves to the east-northeast at about  $15\text{--}20 \text{ m s}^{-1}$ . Maximum winds in the tornado exceed  $80 \text{ m s}^{-1}$  on its southern side. A well-defined tornadic circulation is apparent up to about 2.5 km AGL for tornado 1. However, parcels and vortex lines that enter tornado 1 generally ascend to mid- and upper levels of the storm,

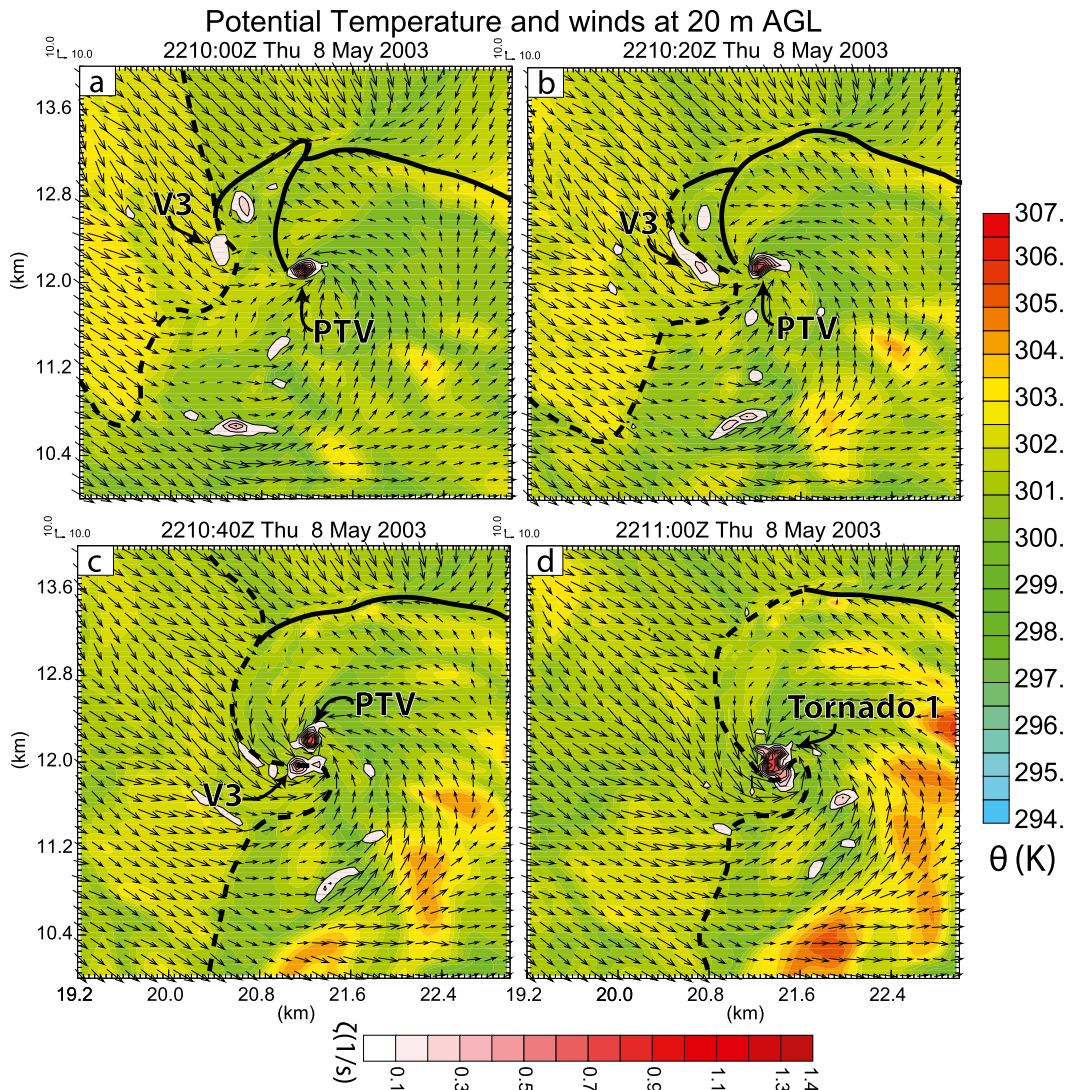


FIG. 7. As in Fig. 6, but at (a) 2210:00, (b) 2210:20, (c) 2210:40, and (d) 2211:00 UTC 8 May 2003.

suggesting a connection with the midlevel updraft (not shown).

Figure 8 shows the evolution of tornado 1 from genesis to just before dissipation (2211–2224 UTC) in terms of near-surface vertical vorticity and can be summarized as follows: After forming, the tornado maintains its intensity for about 4 min. During this period, occasional peaks in intensity (in terms of maximum vorticity) are associated with secondary vortices (e.g., at 2213 UTC) embedded within the tornado (e.g., Lewellen et al. 1997). The tornado then briefly becomes two celled and weakens rapidly (between 2214 and 2215 UTC) as an axial downdraft develops and reaches the surface (not shown). After about 1 min (at 2216 UTC), this weakening trend ceases and the tornado reorganizes about

1 km to the north. The tornado maintains its intensity for about 7 min (again becoming two celled), before dissipating well to the rear of the RFGF at 2224 UTC.

At around 2217 UTC, a few kilometers east of the first tornado, another vertical vorticity maximum (V4) forms just in advance of the RFGF (Figs. 9a,b). The inflow air has cooled owing to cloud shading and occasional light rain in newly developed convective cells. Animations of vertical vorticity (not shown) reveal that V4 initially forms at 2215 UTC as an elongated area of vorticity in association with a new convective cell that has developed in the inflow region of the OKC storm. V4 intensifies rapidly while moving north along the RFGF (Fig. 9c). Over the next minute, V4 continues to strengthen and the wind associated with it reaches

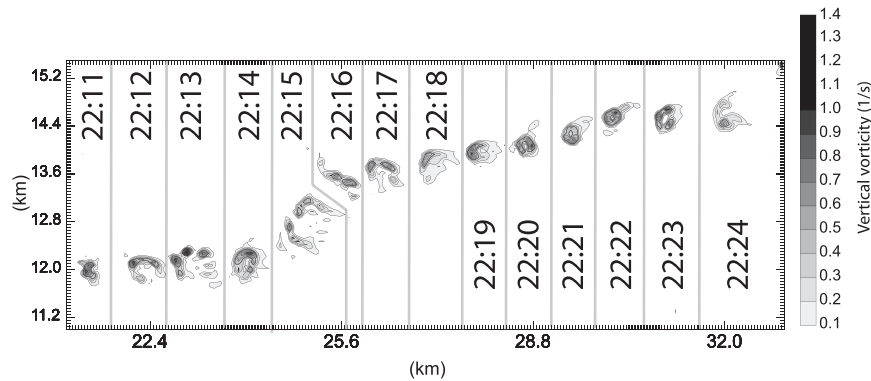


FIG. 8. Overview of the vertical vorticity (shaded greater than  $0.1 \text{ s}^{-1}$ ) at 20 m AGL for tornado 1 plotted each minute between 2211 and 2224 UTC 8 May 2003. Gray lines are added for clarity to indicate which vorticity is associated with which time.

tornadic strength (tornado 2) by 2220 UTC (Fig. 9d). Tornado 2 moves briefly northward and then east-northeastward at about  $20 \text{ m s}^{-1}$  along the FFGF at the occlusion point with the RFGF. Tornado 2 is smaller than tornado 1 and, unlike tornado 1, consists of one vorticity maximum through its entire lifetime. Tornado 2 rapidly weakens below tornado strength after 2225 UTC and dissipates around 2227 UTC. Figure 10 plots the vertical vorticity associated with tornado 2 from the formation of V4 to the dissipation of tornado 2 (2218–2227 UTC). Following the dissipation of tornado 2, the OKC supercell becomes outflow dominant and no additional tornado forms.

### c. Analysis of tornadogenesis

A more detailed analysis is now performed to elucidate the important processes and features responsible for tornadogenesis in the OKC storm simulation. Because they develop quite differently, tornadoes 1 and 2 are discussed separately.

#### 1) DEVELOPMENT OF THE FIRST TORNADO

As described above, tornado 1 developed as a result of the merger of at least three different areas of vertical vorticity (V1–V3). Each of these vorticity centers formed under different circumstances and in different areas of the storm. To determine the origin of V1–V3, backward trajectory, Lagrangian vorticity equation integrations, and vortex line analyses were performed for each vorticity maximum.

The first vorticity maximum to form that was directly related to tornado 1 in the OKC supercell simulation was V1. Inspection of the horizontal vorticity vectors near V1 reveals large ( $>0.1 \text{ s}^{-1}$ ), mainly northward-pointing vorticity vectors at low levels just behind the

RFGF (Fig. 11a). This orientation of the horizontal vorticity vectors is opposite to what would be expected of the vorticity if it were generated baroclinically along the RFGF. Instead, the orientation of the horizontal vorticity is more consistent with it being created by surface drag as the near-surface flow surges to the east behind the RFGF. Moreover, rather than being arched over the RFD, vortex lines that run through V1 are mostly horizontal at the low levels behind the RFGF before rising about 100 m in the updraft along the northern portion of the RFGF (Fig. 11a, with the RFGF extending farther south beyond the southern border of the plot). Vortex lines then descend and can be linked with a weak area of anticyclonic vorticity [near (20.7, 11.6) in Fig. 11a] to the northwest of V1. If vortex lines are extended farther south they eventually rise along southern portions of the RFGF (not shown).

To verify that surface drag is indeed important in generating the northward-pointing horizontal vorticity behind the RFGF in Fig. 11a, vorticity terms and their integrations are calculated along backward trajectories that terminate in and around V1. A fourth-order Runge–Kutta scheme is used to calculate backward trajectories using model output every 2 s. Vorticity integrations are performed that integrate source terms interpolated from the model grid to these trajectories. When a parcel falls below the lowest model scalar point, the vorticity source terms from lowest scalar point are used for the vorticity integration. Because of sensitivities to this methodology of computing source terms near the ground, calculations are done for parcels that terminate in V1 and V3 at 50 and 200 m AGL for V2. Calculations for parcels that terminated below these levels were generally inaccurate as the parcels spent a lot of time near or below the lowest model scalar level.

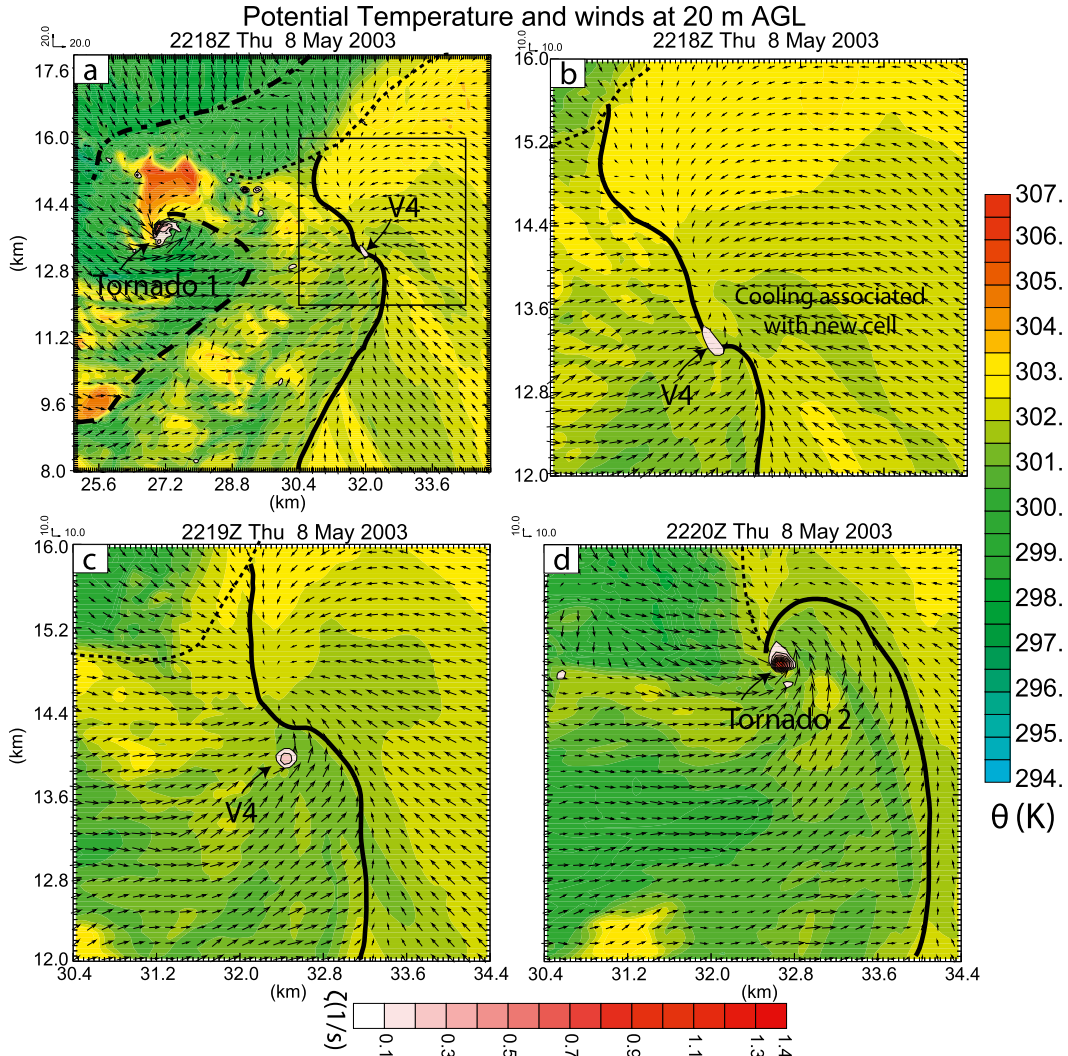


FIG. 9. As in Fig. 6, but for (a) 2218 UTC, and for a zoomed in section of (a) at (b) 2218, (c) 2219, and (d) 2220 UTC. The rectangle in (a) indicates the domain plotted in (b)–(d). The RFGF and FFCB are marked by the thick solid and short dashed lines, respectively. In (a), the long dashed line marks a secondary gust front associated with tornado 1 and the dashed–dotted line marks the location of an internal cold outflow surge from the thunderstorm core.

The vorticity calculations integrate the streamwise,<sup>3</sup> crosswise, and vertical components of vorticity according to the vorticity tendency equations

$$\begin{aligned} \frac{D\omega_s}{Dt} = & \omega_n \frac{D\psi}{Dt} + \boldsymbol{\omega} \cdot \nabla \mathbf{V} + \frac{1}{\rho^2} \left( \frac{\partial \rho}{\partial n} \frac{\partial p}{\partial z} - \frac{\partial \rho}{\partial z} \frac{\partial p}{\partial n} \right) \\ & + \frac{1}{\rho} \left( \frac{\partial F_z}{\partial n} - \frac{\partial F_n}{\partial z} \right), \end{aligned} \quad (1)$$

$$\begin{aligned} \frac{D\omega_n}{Dt} = & -\omega_s \frac{D\psi}{Dt} + \boldsymbol{\omega} \cdot V \nabla \psi + \frac{1}{\rho^2} \left( \frac{\partial \rho}{\partial z} \frac{\partial p}{\partial s} - \frac{\partial \rho}{\partial s} \frac{\partial p}{\partial z} \right) \\ & + \frac{1}{\rho} \left( \frac{\partial F_s}{\partial z} - \frac{\partial F_z}{\partial s} \right), \end{aligned} \quad (2)$$

$$\begin{aligned} \frac{D\zeta}{Dt} = & \zeta \frac{\partial w}{\partial z} + \left( \omega_s \frac{\partial w}{\partial s} + \omega_n \frac{\partial w}{\partial n} \right) + \frac{1}{\rho^2} \left( \frac{\partial \rho}{\partial n} \frac{\partial p}{\partial s} - \frac{\partial \rho}{\partial s} \frac{\partial p}{\partial n} \right) \\ & + \frac{1}{\rho} \left( \frac{\partial F_n}{\partial s} - \frac{\partial F_s}{\partial n} \right), \end{aligned} \quad (3)$$

<sup>3</sup> Streamwise (and crosswise) vorticity is computed with respect to the ground-relative wind.

where  $\psi \equiv \tan^{-1}(v/u)$  and represents the horizontal direction of the parcel;  $V$  is the parcel's speed;  $\rho$  is air density;  $p$  is pressure;  $\omega_s$ ,  $\omega_n$ , and  $\zeta$  are the streamwise,

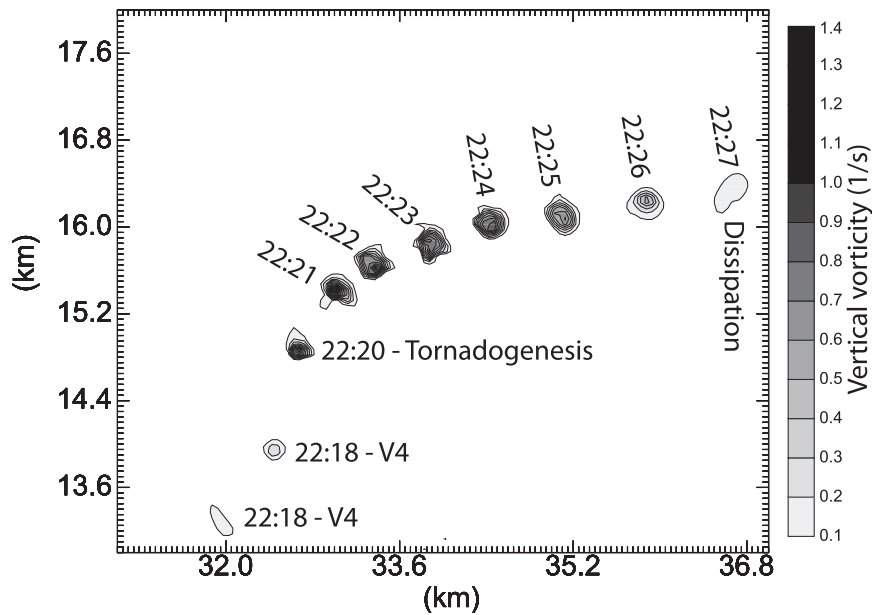


FIG. 10. As in Fig. 8, but for tornado 2 between 2218 and 2227 UTC. Gray lines are omitted because the vorticity pattern is less complicated than for tornado 1.

crosswise, and vertical components of vorticity, respectively; and  $F_s$ ,  $F_n$ , and  $F_z$  are the streamwise, crosswise, and vertical components of the frictional force, respectively. The frictional force in the model interior includes the subgrid-scale turbulence mixing and computational diffusion. The surface drag comes into the system through the frictional force ( $F_s$ ,  $F_n$ ,  $F_z$ ) in the first model layer above ground in the form of surface momentum fluxes, and the vertical momentum flux divergence in that layer causes deceleration owing to surface drag (or negative momentum flux). The surface momentum fluxes are proportional to the local wind speed, the wind components themselves, and to the drag coefficient, with the latter given by a stability-dependent formula. Details can be found in Xue et al. (1995, 2000, 2001).

The first term on the right-hand sides of (1) and (2) represents the exchange of vorticity between the streamwise and crosswise directions owing to changes in the parcel heading. The next three terms in (1) and (2) represent the changes in vorticity from stretching/tilting of vortex tubes, solenoidal generation, and frictional generation, respectively. The terms on the right-hand side of (3) represent vorticity stretching, tilting, solenoidal generation, and frictional generation. To further clarify the origin of vertical vorticity, the two components of the tilting term in (3) are considered separately in our vorticity analysis. Additionally, the Lagrangian-integrated vorticity components from (1)–(3) are compared to the Eulerian-integrated vorticity values (i.e.,

model-predicted gridpoint values) interpolated to the parcel locations (e.g., compare the dark blue and cyan lines in Figs. 12b–d). The parcel trajectory and individual vorticity source calculations are considered reliable when the Eulerian- and Lagrangian-integrated vorticity values are in a good agreement for all three vorticity components along the length of the parcel trajectory.

A representative backward trajectory<sup>4</sup> that enters V1 is plotted in Fig. 12a. Horizontal vorticity calculations along this trajectory (Figs. 12b,c) indeed confirm that frictionally generated vorticity is the dominant term in the total vorticity equation and is likely responsible for much of the large northward-pointing vorticity shown in Fig. 11a. Specifically, as the parcel travels southward near the ground between 2202 and 2205 UTC (Fig. 12a), positive crosswise vorticity  $\omega_c$  is generated by surface drag (Fig. 12c). Between 2205 and 2206 UTC, the parcel rises and turns to the east, leading the exchange term to convert frictionally generated  $\omega_c$  into streamwise vorticity  $\omega_s$ . The parcel then descends with  $\omega_c$  again increasing owing to frictional generation. During this same period,

<sup>4</sup> In this study, representative trajectories are chosen by examining backward trajectories initialized at each model grid point (at a chosen height) within a vorticity maximum. The trajectory chosen to be plotted is generally one in which the vorticity integrations are most accurate with respect to the Eulerian vorticity values. However, the general trends in the vorticity budget are similar for most parcels within the envelope entering a given vorticity maximum.

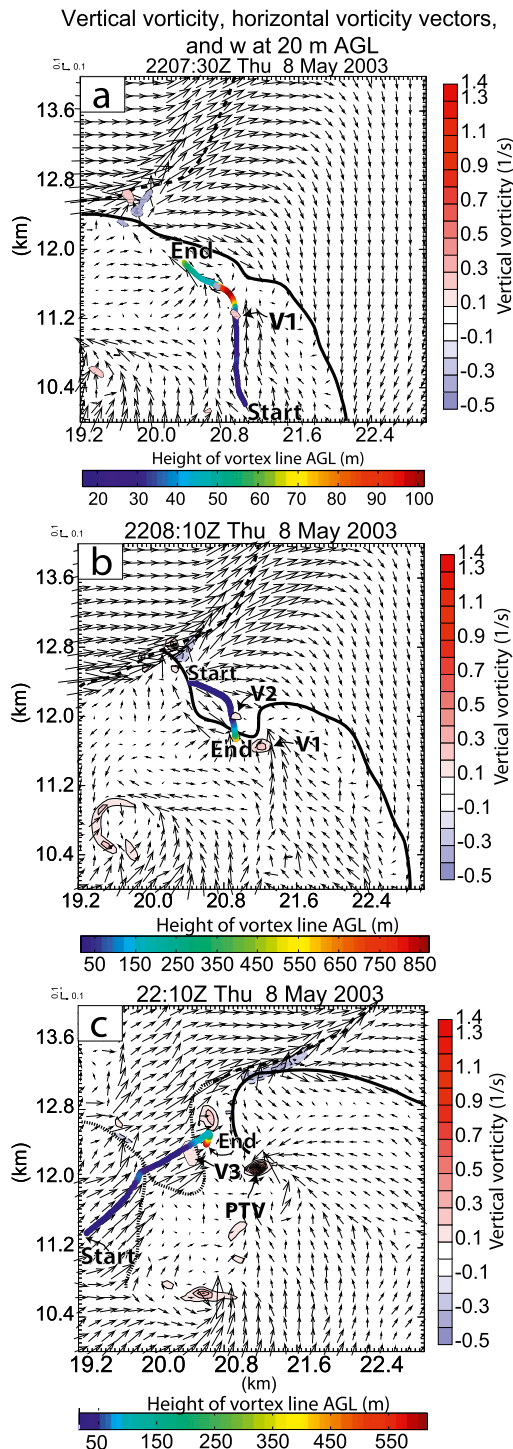


FIG. 11. Vertical vorticity (shaded,  $s^{-1}$ ), horizontal vorticity vectors ( $s^{-1}$ ) at 20 m AGL, and a vortex line that passes through (a) V1 at 2207:3 UTC, (b) V2 at 2208:10 UTC, and (c) V3 at 2210:00 UTC. “Start” and “End” mark the start and end of the segment of the plotted vortex line and are included to indicate the direction of the horizontal vorticity along the vortex line (i.e., pointing from start to end). Plotted area is as in Fig. 6. (Note that the values on the color scale for vortex line height change in each panel.)

$\omega_s$  also increases via a combination of the tilting, stretching, and exchange terms as the parcel continues to turn cyclonically and accelerate. The baroclinic streamwise term is small and generally negative throughout the period examined. The friction term generates substantial negative  $\omega_s$  from 2207 to 2208 UTC. This is a result of friction acting against the cyclonic curvature (cross-stream acceleration) of the parcel during this time period. Positive vertical vorticity  $\zeta$  is first generated via the tilting of  $\omega_s$  from 2206 to 2207:30 UTC (Fig. 12d) as the parcel descends in the RFD. During this same period, tilting of  $\omega_c$  is generally negative. After 2207:30 UTC, additional positive  $\zeta$  is generated via the continued tilting of  $\omega_s$  and stretching as the parcel accelerates upward in the updraft along the RFGF (Fig. 12d).

The trend in  $\zeta$  for the parcel entering V1 is very similar to that discussed in Davies-Jones and Brooks (1993), whereby positive  $\zeta$  first develops in a parcel that is descending in the RFD. Davies-Jones and Brooks (1993) explained that streamwise baroclinic vorticity generation acts to induce slippage between vortex lines and parcel trajectories. This effect allows near-surface positive vertical vorticity to develop as the parcel descends. A similar effect seems to occur for the parcel entering V1 as the inclination angle between vorticity and velocity vectors becomes positive as the parcel begins to descend (Fig. 12e). However, during this period the main vorticity genesis term in the streamwise direction is the exchange term, suggesting that exchange of vorticity from  $\omega_c$  to  $\omega_s$  is responsible for inducing the slippage between the vortex lines and parcel trajectory (the inclination angle also became negative via a similar effect as the parcel was ascending between 2205 and 2206 UTC). Given that much of this  $\omega_c$  was generated via drag, this finding indicates that drag is likely playing a major role in the development of V1. However, it is important to point out that while the trajectory segment shown herein suggests an important role of frictionally generated vorticity, owing to the short time period of integration, it does not rule out the possible importance of baroclinically generated vorticity at earlier times. Parcel integration periods are short by necessity as V1 develops only 7.5 m into the 50-m-grid simulation.

Similar analyses conducted for V2 and V3 found that surface drag again plays an important role in the development of horizontal vorticity that is tilted into the vertical to cause the development of V2 and V3. In the case of V2, near-surface vortex lines that run through V2 point to the east-southeast, which, given the north-northeasterly near-surface wind direction, is consistent with vorticity generated via surface drag. The vortex lines then turn to the south and rise into V2 (Fig. 11b).

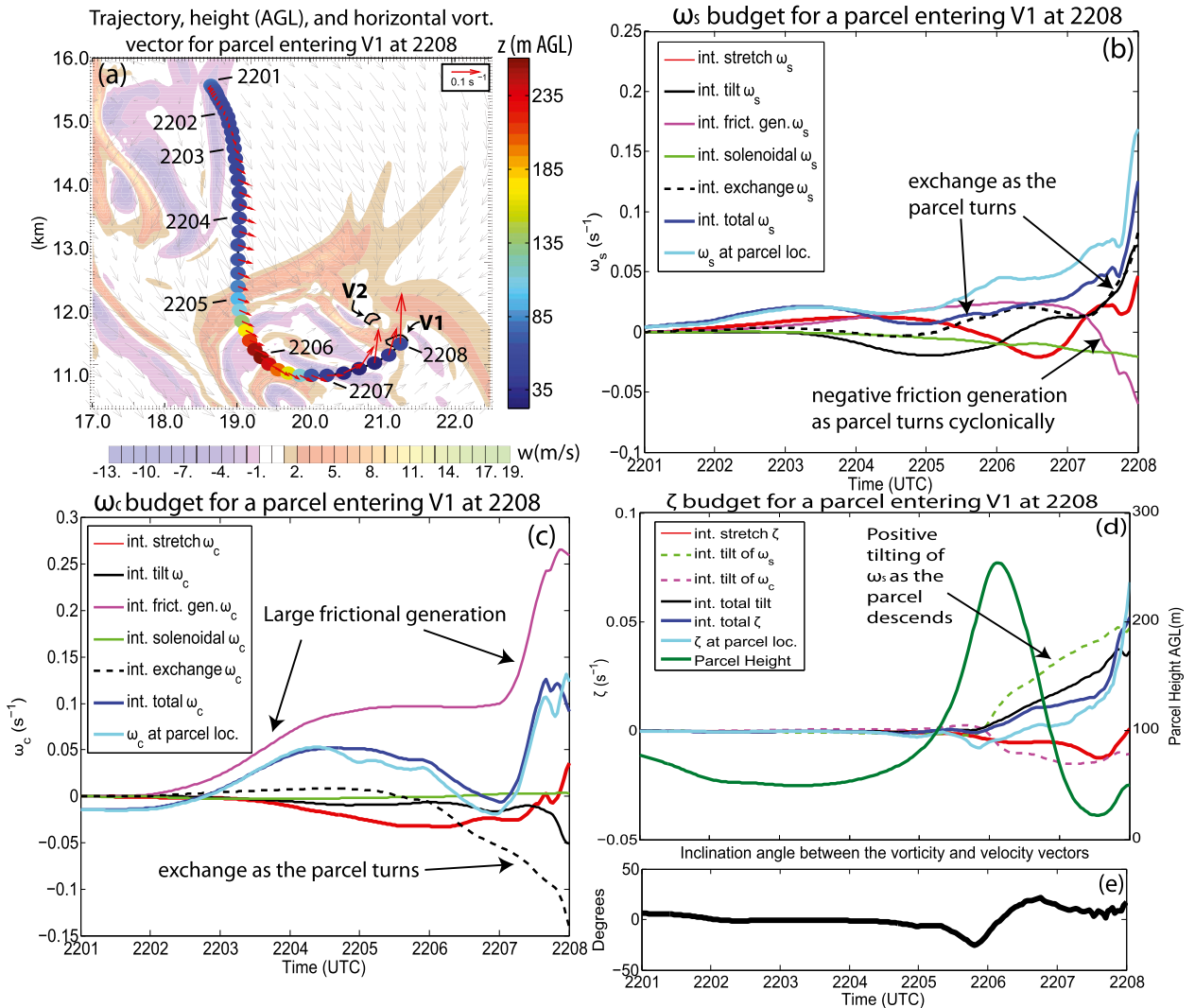


FIG. 12. (a) A representative backward trajectory that terminates at 50 m AGL in V1 at 2208 UTC. Trajectory height (shaded circles, m AGL) and horizontal vorticity (red arrows,  $s^{-1}$ ) are plotted at 10-s increments. The trajectory is overlaid on the vertical velocity (light shading,  $m s^{-1}$ ) and horizontal wind (gray vectors,  $m s^{-1}$ ) at 50 m AGL at 2208 UTC. Also shown are the Lagrangian vorticity integrations along the trajectory plotted in (a) for (b) the horizontal streamwise vorticity, (c) the horizontal crosswise vorticity, and (d) the z-component vorticity. In (b), the dark blue line is the sum of the time-integrated streamwise stretching (red line), tilting (black line), frictional generation (purple line), and baroclinic generation (green line). In (c), the dark blue line is the sum of the time-integrated crosswise stretching (red line), tilting (black line), frictional generation (purple line), and baroclinic generation (green line). In (d), the black line is the sum of the time-integrated tilting of streamwise vorticity (green dashed line) and crosswise vorticity (purple dashed line). The dark blue line in (d) is the sum of the time-integrated z-component stretching (red line) and tilting (black line). The solid green line in (d) represents the height (m AGL) of the parcel. The cyan line represents the value of streamwise [in (b)], crosswise [in (c)], and z-component [in (d)] vorticity interpolated from the model grid to the parcel location at each time. Ideally, the cyan lines match the corresponding blue lines. (e) The inclination between the full vorticity and velocity vectors is plotted.

Calculations along a representative trajectory that enters V2 (Fig. 13a) confirm that the east-southeastward-pointing horizontal vorticity north of V2 (Fig. 11b) was predominantly generated by drag in north-northeasterly low-level flow (Fig. 13c). More specifically, as the parcel moves toward the south-southwest at low levels, large positive  $\omega_c$  is generated by drag between 2201 and

2207 UTC. Around 2206 UTC, the parcel begins to encounter convergence associated with the RFGF, leading to a decrease in the magnitude of the horizontal vorticity through the stretching term. In the streamwise direction (Fig. 13b), the parcel begins with large  $\omega_s$  that gradually increases until 2206 UTC via predominantly stretching and tilting through 2206 UTC. Owing to the short trajectory

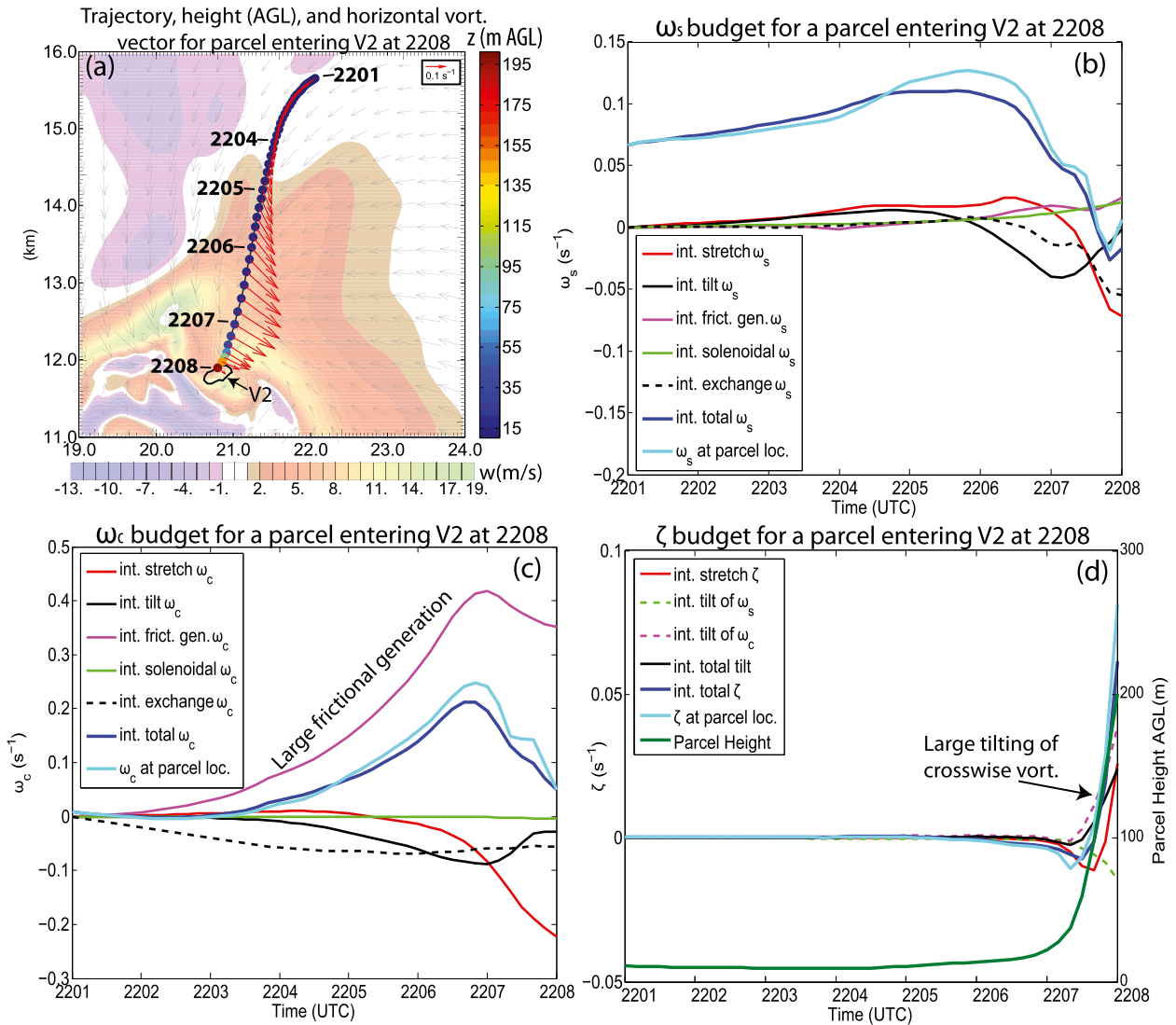


FIG. 13. As in Fig. 12, but without the vorticity inclination panel and for a representative backward trajectory terminating at 200 m AGL in V2 at 2208 UTC. (Note that the values on the color scale for the trajectory height are different than those in Fig. 12.)

integration time, we cannot determine the origin of the parcel's initial  $\omega_s$ . The exchange and stretching term cause  $\omega_s$  to become negative after 2207:30 UTC. The gradient of vertical velocity associated with the RFGF results in the small negative tilting of  $\omega_s$  and large positive tilting of  $\omega_c$  into the vertical (Fig. 13d). Stretching amplifies the positive  $\zeta$  after 2207:30 UTC. It is worth noting that the trajectory plotted in Fig. 13 generates significant vertical vorticity without a downdraft. However, recall that the backward trajectory was initialized 200 m AGL and note that significant vertical vorticity does not develop until the parcel is 100 m AGL (Fig. 13d). As such, these parcels are likely not capturing the mechanism by which near-surface vertical vorticity is developing in V2. Unfortunately, vorticity budgets are highly

inaccurate for parcels that enter V2 below 200 m AGL, limiting our ability to definitively determine the origin of near-surface vorticity in V2. However, as we noted in the previous subsection, V2 increases in intensity with height and first develops about 200 m AGL, leading us to speculate that near-surface vorticity in V2 may be generated by vertical diffusion in the model.

As noted in the previous subsection, tornadogenesis is coincident with the arrival of the internal surge. Large northeastward-pointing horizontal vorticity is present at low levels within this internal surge (Fig. 11c). Vortex lines near the ground point northeastward in the internal RFD surge and then turn upward along the northern side of the internal surge gust front (Fig. 11c).

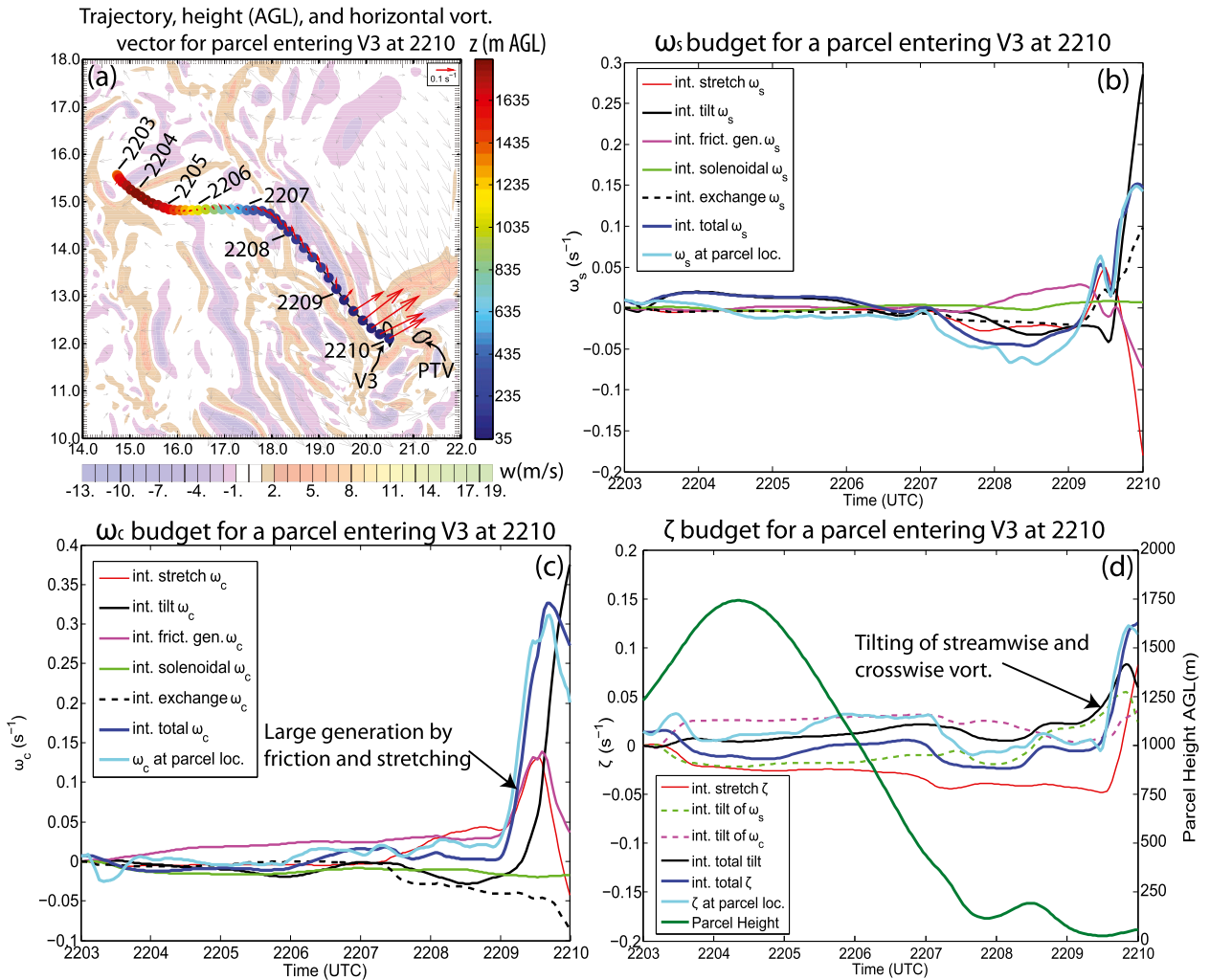


FIG. 14. As in Fig. 13, but for a representative backward trajectory terminating in V3 at 2210 UTC. (Note that the values on the color scale for the trajectory height are different than those in Fig. 12.)

A representative backward trajectory that terminates in V3 is plotted in Fig. 14a. Vorticity integrations along this trajectory suggest that large  $\omega_s$  and  $\omega_c$  are generated as the parcel descends below 100 m AGL (Figs. 14b,c). The  $\omega_c$  is generated primarily via surface drag and horizontal stretching (Fig. 14c) and the exchange term concurrently converts this  $\omega_c$  into the streamwise direction (Fig. 14b). The  $\omega_s$  is also enhanced by stretching from 2209:00 to 2209:30 UTC and tilting from 2209:30 to 2210:00 UTC. Positive vertical vorticity is generated predominantly after 2209 UTC via the tilting of both  $\omega_s$  and  $\omega_c$  as the descending parcel approaches its nadir (Fig. 14d). Starting at 2209:30 UTC, the parcel's vertical vorticity is amplified via stretching in the updraft along the leading edge of the internal RFD surge intensifying V3 (Fig. 14d). Attempts to examine the inclination angle between vorticity and velocity for the parcel entering V3

(not shown) were inconclusive as the parcel had non-negligible vertical vorticity throughout the backward integration.

As the internal RFD surge approaches the low-level updraft associated with the PTV, V3 dramatically amplifies as seen in Figs. 7b and 7c. Tornadogenesis occurs as V3 (and the internal RFD surge) combines with the PTV. As these features merge, low-level horizontal vorticity vectors within the internal RFD surge, which initially are mainly crosswise to the flow (because the vorticity is predominantly frictionally generated), become increasingly streamwise as the flow develops a radially inward component toward the developing tornado (Figs. 15a,b). Vorticity calculations along a forward parcel trajectory that enters tornado 1 suggest that ingestion of this streamwise vorticity is important in the amplification of  $\zeta$  in tornado 1 as there is large tilting of

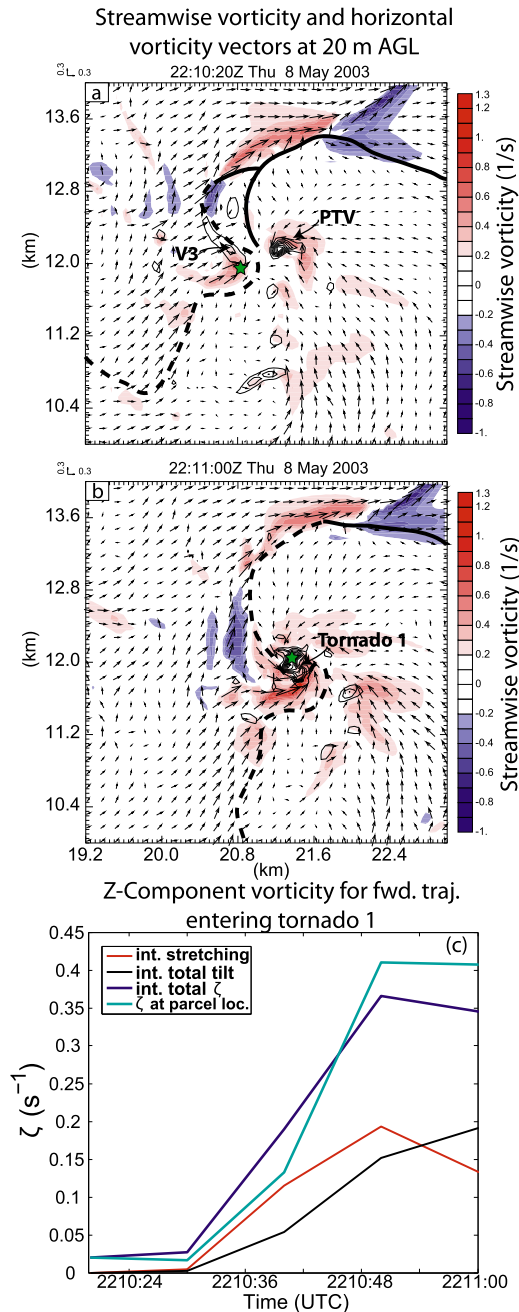


FIG. 15. Streamwise vorticity (shaded,  $s^{-1}$ ), vertical vorticity (contoured,  $s^{-1}$ ), and horizontal vorticity vectors ( $s^{-1}$ ) at (a) 2210:20 and (b) 2211:00 UTC. The green star in (a) and (b) marks the start and end location of a forward trajectory, respectively. (c) A vertical vorticity budget for this parcel. The dark blue line is the sum of the time-integrated stretching (red line) and tilting (black line). The cyan line is the model value of vertical vorticity interpolated to the parcel location at each time.

parcel's horizontal vorticity into the vertical as it flows into the developing tornado (Fig. 15c).

The above result supports the findings of recent studies that emphasize the important role played by internal

RFD surges in tornadogenesis and/or maintenance (Mashiko et al. 2009; Marquis et al. 2012; Lee et al. 2012). Marquis et al. (2012) concluded that these internal surges may be important because they increase low-level convergence and augment the vertical vorticity of the tornado via tilting of baroclinically generated horizontal vorticity along the internal surge gust front. Meanwhile, Mashiko et al. (2009) suggested that the internal RFD surge brought large environmental streamwise vorticity to the ground and into the tornado. In our case, mechanically generated vorticity via surface drag in the internal RFD surge is an important contributor to the horizontal vorticity that later gets tilted into vertical and stretched to form intense vortices. It is worth noting that, unlike the studies mentioned above, the mechanism by which the internal surge plays an important role in the present case does not rely on the internal surge being very cold nor on the environment containing large vorticity. This finding is significant given the large variability in the thermodynamic characteristics of observed internal RFD surges (e.g., Lee et al. 2012) and the fact that extreme low-level shear like that seen in the tropical cyclone environment of Mashiko et al. (2009) is not typically observed in classic supercell environments.

## 2) DEVELOPMENT OF THE SECOND TORNADO

As mentioned above, the development of tornado 2 was somewhat less complex than that of tornado 1 with only one important vertical vorticity maximum contributing to tornado 2. This vertical vorticity maximum, V4, developed about 5 km to the east of the RFGF as a stronger surge of inflow<sup>5</sup> air moved toward the RFGF (Fig. 9b). The stronger surge of inflow air was associated with a new convective cell that developed in advance of the RFGF (not shown). This evolution resembles the case described in Wakimoto and Atkins (1996) in which a tornado developed rapidly in association with a new convective cell that formed along the flanking line of a mature supercell. On the storm scale, this evolution also resembles the type-II descending reflectivity core (DRC) scenario presented in Byko et al. (2009), with V4 developing between stages 3 and 4 of their conceptual model. More specifically, V4 intensifies as the new convective cell encountered the RFGF and began to merge with the main updraft of the OKC storm.

To investigate further the development of V4 and tornado 2, a trajectory and vortex line analysis was

<sup>5</sup> Inflow is defined with respect to the main OKC storm. As such, we consider the momentum surge associated with the new cell to be an inflow surge even though it is rain cooled and has descended slightly.

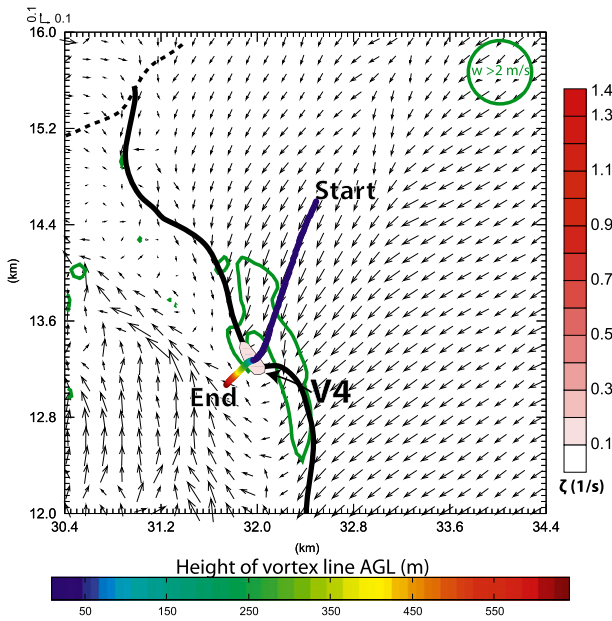


FIG. 16. As in Fig. 11, but for a vortex line entering V4 at 20 m AGL at 2218 UTC. Green contours mark areas where vertical velocity is greater than  $2 \text{ m s}^{-1}$ . Plotted area is as in Fig. 9b. (Note that values on the color scale for the vortex line height are different than those in Fig. 11.)

performed. This analysis reveals that, at low levels, horizontal vorticity vectors in the inflow surge associated with the new updraft point toward the southwest (Fig. 16). Vortex lines that pass through V4 are horizontal, pointing to the southwest, before rising abruptly as they encounter the RFGF (Fig. 16). Backward trajectory analysis indicates that parcels that enter V4 come from the southeast at low levels, gradually descend, and then rise as they encounter the RFGF, as shown by a representative parcel in Fig. 17a. Vorticity calculations along the trajectory shown in Fig. 17a indicate that the parcel acquires substantial  $\omega_s$  and  $\omega_c$  as it moves toward V4 (Figs. 17b,c). In the streamwise direction, large positive  $\omega_s$  generation by tilting is offset by large negative  $\omega_s$  generation by friction (Fig. 17b). The exchange and stretching terms are both positive and result in the parcel developing large  $\omega_s$  by 2217. This  $\omega_s$  is then diminished by convergence along the RFGF (negative stretching) and by the exchange term as the parcel turns to the north. In the crosswise direction, vorticity is generated via stretching of environmental vorticity<sup>6</sup> between 2208 and 2212 UTC and

<sup>6</sup> It is likely that much of this environmental vorticity is frictionally generated as a shallow layer of large horizontal vorticity is present near the surface in the inflow (see Fig. 4).

via surface drag between 2210 and 2217 UTC (Fig. 17c). Nearly all of the  $\omega_c$  is removed by large negative stretching as the parcel encounters the RFGF after 2217 UTC. The vertical vorticity budget (Fig. 17d) indicates that positive vertical vorticity first develops around 2210 UTC via tilting of crosswise vorticity as the parcel descends in the rain core of the new convective cell. Vertical vorticity is then amplified dramatically by stretching as the parcel encounters the strong convergence/updraft along the RFGF.

Between 2218 and 2220 UTC, V4 continues to strengthen as it moves northward (see Fig. 9). During this time period, V4 is located on the southern edge of a low-level updraft maximum along the RFGF (Fig. 18a). Around 2220 UTC, V4 becomes better collocated with the low-level updraft and reaches tornadic strength (Fig. 18b). An area of strong westerly flow develops to the south and west of tornado 2 with large frictionally generated northward-pointing vorticity (Figs. 18a,b). This vorticity begins crosswise but becomes streamwise as the flow accelerates radially inward toward tornado 2 (Fig. 18c). This streamwise vorticity is then tilted and stretched, aiding in the intensification of the developing tornado. This is somewhat similar to the role played by the internal RFD surge that was associated with the generation of tornado 1. However, unlike the earlier internal RFD surge, the internal surge of westerly momentum associated with tornado 2 cannot be traced far upstream and, instead, appears to develop in situ as the flow accelerates in response to the development of tornado 2 and associated low-level updraft.

*d. Free-slip simulation*

In attempt to verify the important role surface drag played in the simulation discussed above, the simulation was rerun with the mechanical drag coefficient set to zero. As in the simulation of the 8–9 May 2007 tornadic mesovortex presented in Schenkman et al. (2012), only the innermost grid (in the present case, the 50-m grid-spacing domain) was rerun with drag turned off. Boundary and initial conditions from the 100-m simulation at 2200 UTC are still impacted by the surface drag. However, given that the tornadoes and low-level structure of the supercell developed largely during the simulation on the 50-m-grid-spacing domain [and that extracted soundings from various points in the storm inflow suggest much of the enhanced low-level shear associated with surface drag dissipates in about 5 min of model integration (not shown)], it is assumed that the impact of drag from the boundary and initial conditions should be relatively small.

Comparison of the no-drag and drag simulations reveals considerable differences. Not surprisingly, the

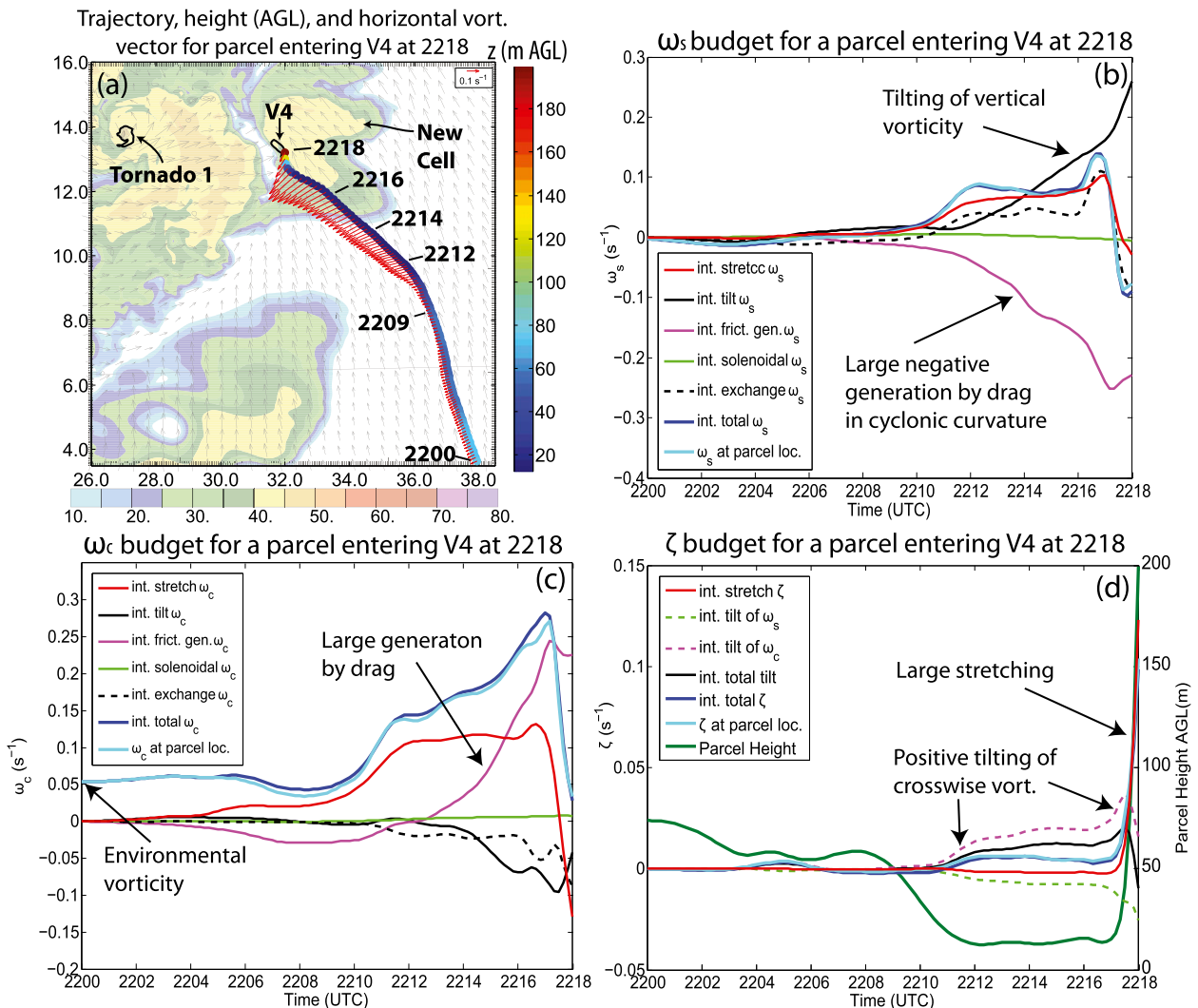


FIG. 17. As in Fig. 13, but for a representative backward trajectory terminating at 200 m AGL in V4 at 2218 UTC. (a) Trajectory is overlaid on simulated radar reflectivity factor (dBZ) rather than vertical velocity as in Fig. 12. (Note that the values on the color scale for the trajectory height are different than those in Fig. 12.)

largest differences in the simulations involve the low-level wind field. Specifically, the RFGF structure is substantially different with a less distinct RFGF in the no-drag experiment (Fig. 19a). Additionally, though a tornado does develop in the no-drag simulation (tornado ND1), it is much shorter lived than tornado 1 in the drag simulation. Tornado ND1 follows a very different path than tornado 1, initially moving northeast before suddenly turning to the west and then southeast before dissipating (Fig. 20). The maximum wind speeds in the no-drag simulation tornado are briefly the same strength those in the drag simulation; however, it appears that these winds may be primarily caused by a strong occlusion downdraft that develops to the northeast of tornado ND1 (not shown). This downdraft is also responsible for

the westward motion of the tornado ND1. Tornado ND1 then weakens while being pushed to the southeast by a cold internal outflow surge (not shown). No additional tornadoes form after the dissipation of tornado ND1.

Closer examination of the formation of tornado ND1 reveals that it originated around 2206 UTC as a small vorticity maximum along the leading edge of an outflow surge (Fig. 21). A vortex line and trajectory analysis was performed in order to determine the origin of this vertical vorticity. The vortex line analysis shows that southeastward-pointing horizontal vortex lines within the outflow surge tilt upward, turn toward the southwest, and arch over the outflow surge, creating a vorticity couplet (Fig. 21). The northern cyclonic member of this couplet is the vorticity maximum that becomes tornado

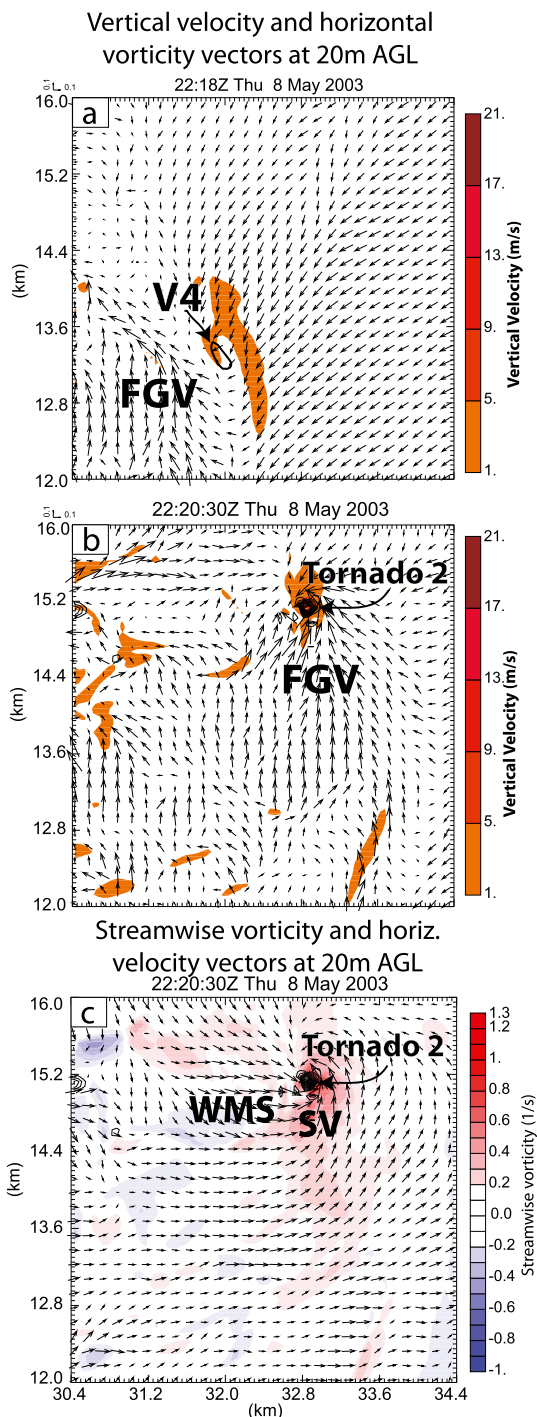


FIG. 18. Vertical velocity (shaded,  $\text{m s}^{-1}$ ), horizontal vorticity vectors ( $\text{s}^{-1}$ ), and vertical vorticity (black contours,  $\text{s}^{-1}$ ) at 20m AGL at (a) 2218:00 and (b) 2220:30 UTC. (c) The same area is shown, but with streamwise vorticity (shaded,  $\text{s}^{-1}$ ) and horizontal wind vectors instead of vertical velocity and horizontal vorticity vectors, respectively, plotted at 2220:30 UTC. “FGV” in (a) and “SV” in (b) mark locations of large frictionally generated vorticity and streamwise vorticity, respectively. In (c), “WMS” marks the locations of the westerly momentum surge into the tornado.

ND1. The southern anticyclonic member of the couplet dissipates with time.

Lagrangian vorticity integrations along backward trajectories that enter tornado ND1 were examined in order to determine the origin of the horizontal vorticity that was tilted into the developing tornado. Unfortunately, this analysis proved inconclusive as large differences were found between the Lagrangian-integrated vorticity source terms and the Eulerian-interpolated vorticity values. This suggests that the backward trajectory and/or the associated vorticity term calculations for these trajectories were unreliable. It is unclear why the calculations were less accurate for the no-drag simulation; it may be related to very large horizontal accelerations when the air parcels are suddenly freed from significant surface drag. Large speed and/or directional accelerations tend to reduce the accuracy of trajectory calculations.

Given the lack of accurate trajectory calculations, our conclusions about the origin of vorticity in tornado ND1 must contain a degree of speculation. However, we note that the vorticity along and behind the RFGF and FFCB generally contains a northerly component. In contrast, the environmental vorticity is generally from the southeast. This difference in the vorticity vector orientation as well the presence of the vortex arch suggests that baroclinic vorticity generation is likely playing an important role in the generation of tornado ND1. Vorticity calculations along backward trajectories in the vicinity of tornado ND1 (~1 km upstream of the tornado) within the outflow surge were much more accurate (with the Lagrangian and Eulerian values matching more closely) than those that were initiated within the developing tornado. Unfortunately, owing to temporal proximity of tornadogenesis to model start time it is not possible to extend these parcel calculations backward far enough using the 50-m-simulation data to confirm that baroclinic vorticity generation is responsible for the northerly vorticity component.

If indeed baroclinity is playing an important role in tornadogenesis in the no-drag simulation, then an obvious question emerges: What role does baroclinity play in tornadogenesis in the drag simulation? To answer this question unambiguously would require integration of representative trajectories and vorticity forcings all the way back to the inflow region. Because of the small domain and short time integration of the 50-m grid, this is difficult to do with the current simulation. Moreover, because there is not a one-to-one correspondence between important features in the drag and no-drag simulation (e.g., tornado 1 develops via the combinations of three separate vorticity maxima whereas tornado ND1 forms from a single maximum), it is difficult to make

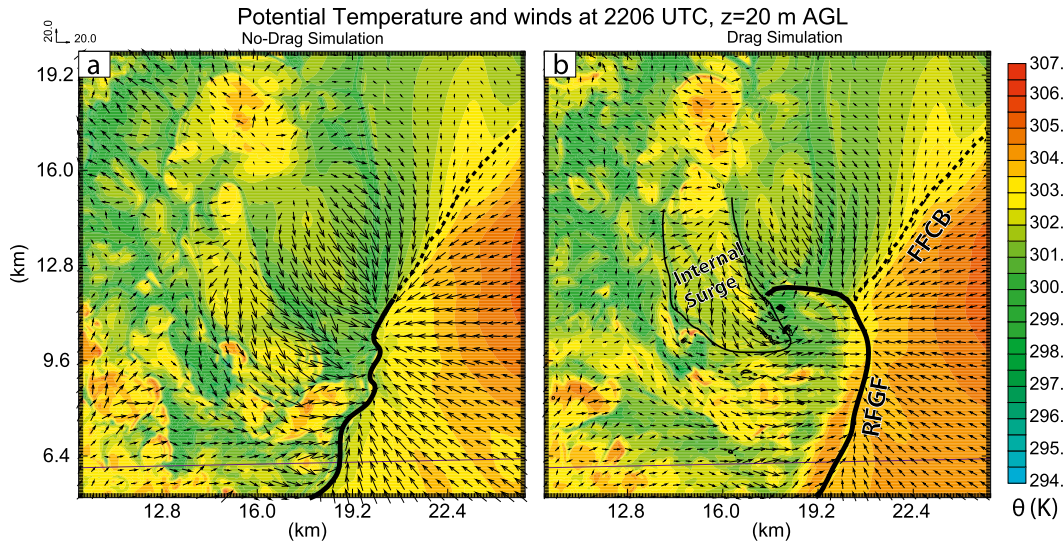


FIG. 19. As in Fig. 5b, but for (a) the no-drag run for comparison with (b) a reproduction of Fig. 5b.

direct comparisons between the two simulations. Finally, because the free-slip simulation's initial and boundary conditions were impacted by surface drag, we cannot rule out the possibility that tornadogenesis in the free-slip simulation was influenced by surface drag. The previous subsection presented considerable evidence that surface drag is playing a major role in the final stage preceding tornadogenesis in the drag simulation, but partitioning its role relative to baroclinic processes will require future work.

**5. Summary and discussion**

Tornadogenesis was investigated in a high-resolution simulation of the 8 May 2003 Oklahoma City tornadic supercell. The simulation, which featured 50-m horizontal grid spacing, was one-way nested within three

coarser-resolution simulations. The outermost domain had 9-km grid spacing and assimilated conventional observations via Advanced Regional Prediction System (ARPS) 3DVAR. ARPS 3DVAR was also used in 5-min data assimilation cycles to assimilate radar data onto a 1-km-grid-spacing domain that was nested within the 9-km domain. The 1-km-grid-spacing domain provided boundary and initial conditions for a nested 100-m-grid-spacing domain. Boundary and initial conditions for the 50-m-grid-spacing simulation were obtained from this 100-m grid 20 min into its simulation.

Two tornadoes developed in the 50-m-grid-spacing simulation (tornado 1 and tornado 2). Both of these tornadoes tracked within 10 km of the observed OKC tornado. Analyses of the model fields, vortex lines, and backward trajectories were conducted to elucidate the

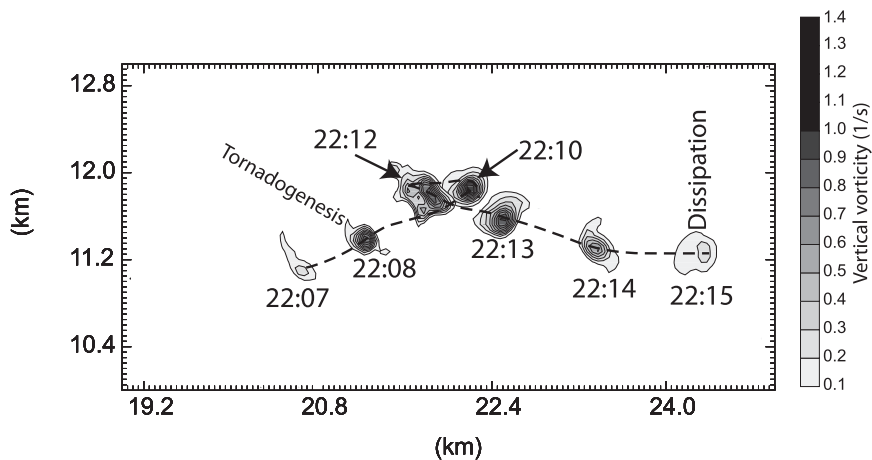


FIG. 20. As in Fig. 8, but for tornado ND1. For clarity, a dashed line is included to mark the track of tornado ND1.

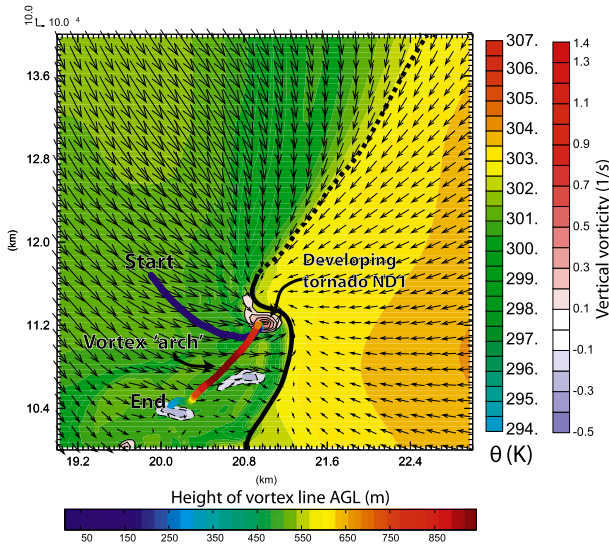


FIG. 21. As in Fig. 11, but also overlaid on potential temperature (shaded, K) and for a vortex line entering tornado ND1 20 m AGL at 2207:30 UTC.

important processes responsible for the genesis of tornadoes 1 and 2. Conceptual models are now presented that summarize the results of the analyses. The conceptual model for tornado 1 (Fig. 22) has three stages and can be summarized as follows:

- (i) The RFD becomes organized with the development of a well-defined RFGF. Large, predominantly frictionally generated vorticity develops behind the RFGF at low levels. This vorticity is tilted into the vertical as parcels descend in the northern edge of the RFGF, leading to the formation of a small vertical vorticity maximum (V1). Concurrently, large eastward-pointing horizontal vorticity is frictionally generated in low-level northerly flow behind the FFCB. As parcels are forced to rise upon encountering the RFGF, this vorticity is tilted and another small vertical vorticity maximum (V2) forms near the intersection of the RFGF and FFGF. V2 is strongest and first forms slightly above the ground.
- (ii) The two areas of vorticity described in (i) merge to form a pretornadic vortex (PTV). At the same time, an internal RFD surge, which is the result of water loading in the core of the supercell, moves quickly southeastward toward the PTV. Large northeastward-pointing horizontal vorticity is generated predominantly by surface drag at low levels within the internal RFD surge. Vertical vorticity is generated as parcels descend in the internal surge, creating a third vorticity maximum (V3) on the northeastern side of the internal surge (V3).

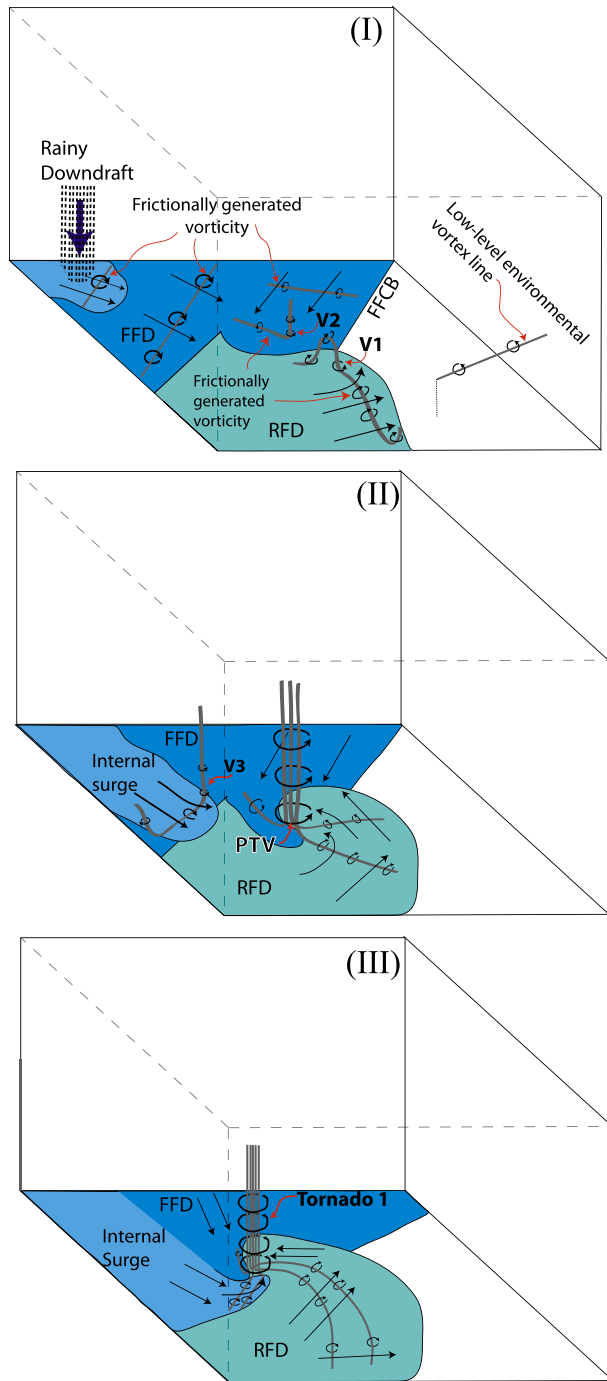


FIG. 22. Three-stage conceptual model for the genesis of tornado 1. Gray lines are vortex lines; black vectors are the horizontal wind. The shades of blue from lightest to darkest represent the RFD, internal outflow surge, and FFD.

- (iii) The internal RFD surge and the merger of V3 with the PTV trigger tornadogenesis by enhancing low-level convergence and providing a substantial source of horizontal vorticity that is readily ingested into the developing tornado.

Although its development differs substantially from tornado 1, the development of tornado 2 is also well described by a three-step conceptual model (Fig. 23). This model can be described as follows:

- (i) A new convective cell develops to the southeast of the supercell. The new cell is associated with accelerating southeasterly low-level flow, which acts to stretch preexisting environmental vorticity and new frictionally generated horizontal vorticity. Weak downdrafts associated with the new convective cell cause parcels to descend as the new cell moves toward the RFGF of the OKC supercell. An elongated area of weak vertical vorticity is generated in this descending flow.
- (ii) The elongated area of vorticity intensifies and consolidates into a vertical vorticity maximum (V4) as the new convective cell (and associated southeasterly low level) encounters the RFGF of the OKC supercell.
- (iii) The vertical vorticity maximum strengthens as it becomes better collocated with the updraft of the OKC supercell, leading to more intense vertical stretching. Concurrently, large frictionally generated crosswise horizontal vorticity develops beneath enhanced westerly flow on the southern side of the tornado. This vorticity becomes streamwise as the flow turns radially inward toward the tornado. Rapid intensification to tornado strength occurs owing to the combination of these effects.

The substantial impact of surface drag in the genesis of both tornadoes prompted the execution of a simulation in which the surface drag coefficient was set to zero. Even though a tornado still formed in the no-drag simulation, substantial differences in the evolution of tornadogenesis between the no-drag simulation and the drag simulation confirm the large impact of surface drag on the simulation. Additionally, the no-drag simulation featured only one tornado that was shorter lived and took a substantially different track than the tornadoes in the drag simulation. Vortex line analyses (which revealed the development of vortex arches over the RFD) suggest that the baroclinicity may have played an important role in the no-drag simulation. However, it was not possible to conclusively determine the relative roles of baroclinic and barotropic (environmental) vorticity.

Perhaps the most significant finding of the present study was the important role played by surface drag in the origin of vertical vorticity near the ground in the drag simulation. It is important not to overemphasize the exact steps in the conceptual model for tornado 1, as the exact evolution in tornadogenesis is likely strongly

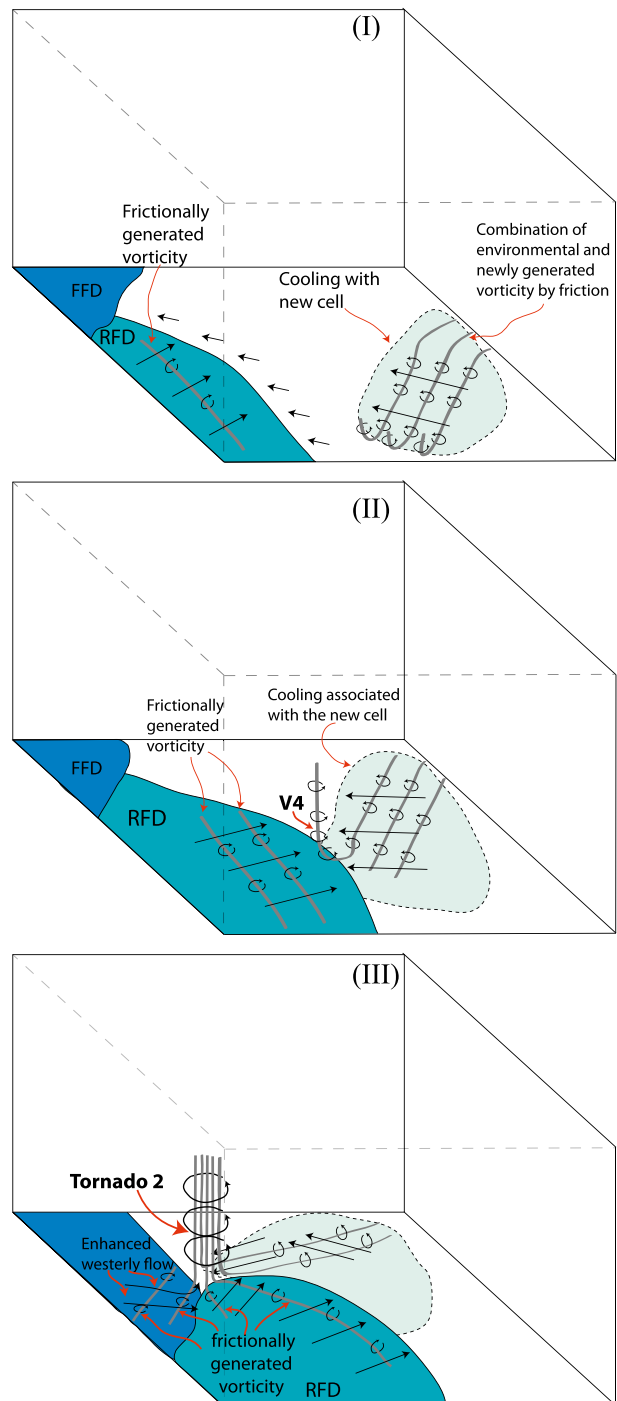


FIG. 23. As in Fig. 22, but for tornado 2. The light blue shading indicates cooling associated with a new convective cell.

case dependent; more important is the general process whereby predominantly frictionally generated vorticity was reoriented into the vertical to generate near-surface vertical vorticity. To the authors' knowledge, the present study represents the first time that this role of surface

drag has been quantified and implicated in tornado-genesis [although Markowski et al. (2012b) pointed out that they could not rule out the aggregate effects of viscosity on the development of low-level rotation in their observation study]. Future work should examine additional tornado cases, again through high-resolution simulations that include realistic drag parameterization, to examine whether surface drag plays a similar role and, thus, assess the generality of the findings of the present study. Idealized experiments should also be conducted in order to determine the importance of frictionally generated vorticity relative to baroclinic and barotropic vorticity.

*Acknowledgments.* This work was primarily supported by NSF Grant AGS-0802888. The second author was also supported by NSF Grants EEC-0313747, OCI-0905040, AGS-0750790, AGS-0941491, AGS-1046171, and AGS-1046081. Numerical simulations were performed at the University of Oklahoma Supercomputing Center for Education and Research (OSCER) and on a national XSEDE supercomputer at the National Institute of Computational Science (NICS) at the University of Tennessee. The first author thanks Brett Roberts, Drs. Matthew Kumjian, and Daniel Dawson for discussions about the analyses presented herein. Comments and suggestions from Dr. Paul Markowski and two anonymous reviewers were very helpful in improving the interpretation of results.

#### REFERENCES

- Beck, J., and C. C. Weiss, 2013: An assessment of low-level baroclinity and vorticity within a simulated supercell. *Mon. Wea. Rev.*, **141**, 649–669.
- Browning, K. A., 1962: The cellular structure of convective storms. *Meteor. Mag.*, **91**, 341–350.
- Byko, Z., P. M. Markowski, Y. Richardson, J. Wurman, and E. Adlerman, 2009: Descending reflectivity cores in supercell thunderstorms observed by mobile radars and in a high-resolution numerical simulation. *Wea. Forecasting*, **24**, 155–186.
- Byun, D. W., 1990: On the analytical solutions of flux-profile relationships for the atmospheric surface layer. *J. Appl. Meteor.*, **29**, 652–657.
- Chow, F. K., R. L. Street, M. Xue, and J. H. Ferziger, 2005: Explicit filtering and reconstruction turbulence modeling for large-eddy simulation of neutral boundary layer flow. *J. Atmos. Sci.*, **62**, 2058–2077.
- Davies-Jones, R., 1984: Streamwise vorticity: The origin of updraft rotation in supercell storms. *J. Atmos. Sci.*, **41**, 2991–3006.
- , and H. E. Brooks, 1993: Mesocyclogenesis from a theoretical perspective. *The Tornado: Its Structure, Dynamics, Prediction, and Hazards*, *Geophys. Monogr.*, Vol. 79, Amer. Geophys. Union, 105–114.
- Dowell, D. C., and L. J. Wicker, 2009: Additive noise for storm-scale ensemble data assimilation. *J. Atmos. Oceanic Technol.*, **26**, 911–927.
- , —, and C. Snyder, 2011: Ensemble Kalman filter assimilation of radar observations of the 8 May 2003 Oklahoma City supercell: Influence of reflectivity observations on storm-scale analysis. *Mon. Wea. Rev.*, **139**, 272–294.
- Gao, J., and D. J. Stensrud, 2012: Assimilation of reflectivity data in a convective-scale, cycled 3DVAR framework with hydro-meteor classification. *J. Atmos. Sci.*, **69**, 1054–1065.
- , M. Xue, K. Brewster, and K. K. Droegemeier, 2004: A three-dimensional variational data analysis method with recursive filter for Doppler radars. *J. Atmos. Oceanic Technol.*, **21**, 457–469.
- Grzych, M. L., B. D. Lee, and C. A. Finley, 2007: Thermodynamic analysis of supercell rear-flank downdrafts from Project ANSWERS. *Mon. Wea. Rev.*, **135**, 240–246.
- Hamill, T. M., R. S. Schneider, H. E. Brooks, G. S. Forbes, H. B. Bluestein, M. Steinberg, D. Melendez, and R. M. Dole, 2005: The May 2003 extended tornado outbreak. *Bull. Amer. Meteor. Soc.*, **86**, 531–542.
- Hirth, B. D., J. L. Schroeder, and C. C. Weiss, 2008: Surface analysis of the rear-flank downdraft outflow in two tornadic supercells. *Mon. Wea. Rev.*, **136**, 2344–2363.
- Hu, M., and M. Xue, 2007: Impact of configurations of rapid intermittent assimilation of WSR-88D radar data for the 8 May 2003 Oklahoma City tornadic thunderstorm case. *Mon. Wea. Rev.*, **135**, 507–525.
- , —, and K. Brewster, 2006a: 3DVAR and cloud analysis with WSR-88D level-II data for the prediction of Fort Worth tornadic thunderstorms. Part I: Cloud analysis and its impact. *Mon. Wea. Rev.*, **134**, 675–698.
- , —, J. Gao, and K. Brewster, 2006b: 3DVAR and cloud analysis with WSR-88D level-II data for the prediction of Fort Worth tornadic thunderstorms. Part II: Impact of radial velocity analysis via 3DVAR. *Mon. Wea. Rev.*, **134**, 699–721.
- Klemp, J. B., and R. B. Wilhelmson, 1978a: Simulations of right- and left-moving thunderstorms produced through storm splitting. *J. Atmos. Sci.*, **35**, 1097–1110.
- , and —, 1978b: The simulation of three-dimensional convective storm dynamics. *J. Atmos. Sci.*, **35**, 1070–1096.
- , and R. Rotunno, 1983: A study of the tornadic region within a supercell thunderstorm. *J. Atmos. Sci.*, **40**, 359–377.
- , R. B. Wilhelmson, and P. S. Ray, 1981: Observed and numerically simulated structure of a mature supercell thunderstorm. *J. Atmos. Sci.*, **38**, 1558–1580.
- Kumjian, M. R., and A. V. Ryzhkov, 2009: Storm-relative helicity revealed from polarimetric radar measurements. *J. Atmos. Sci.*, **66**, 667–685.
- Lee, B. D., C. A. Finley, and T. M. Samaras, 2011: Surface analysis near and within the Tipton, Kansas, tornado on 29 May 2008. *Mon. Wea. Rev.*, **139**, 370–386.
- , —, and C. D. Karstens, 2012: The Bowdle, South Dakota, cyclic tornadic supercell of 22 May 2012: Surface analysis of rear-flank downdraft evolution and multiple internal surges. *Mon. Wea. Rev.*, **140**, 3419–3441.
- Lewellen, W. S., D. C. Lewellen, and R. I. Sykes, 1997: Large-eddy simulation of a tornado's interaction with the surface. *J. Atmos. Sci.*, **54**, 581–605.
- Liu, S., M. Xue, and Q. Xu, 2007: Using wavelet analysis to detect tornadoes from Doppler radar radial-velocity observations. *J. Atmos. Oceanic Technol.*, **24**, 344–359.
- Markowski, P. M., and Y. Richardson, 2009: Tornado-genesis: Our current understanding, forecasting considerations, and questions to guide future research. *Atmos. Res.*, **93**, 3–10.
- , J. M. Straka, and E. N. Rasmussen, 2002: Direct surface thermodynamic observations within the rear-flank downdrafts

- of nontornadic and tornadic supercells. *Mon. Wea. Rev.*, **130**, 1692–1721.
- , E. Rasmussen, J. Straka, R. Davies-Jones, Y. Richardson, and R. J. Trapp, 2008: Vortex lines within low-level mesocyclones obtained from pseudo-dual-Doppler radar observations. *Mon. Wea. Rev.*, **136**, 3513–3535.
- , M. Majcen, Y. Richardson, J. Marquis, and J. Wurman, 2011: Characteristics of the wind field in a trio of nontornadic low-level mesocyclones observed by the Doppler on wheels radars. *Electron. J. Severe Storms Meteor.*, **6** (3). [Available online at <http://www.ejssm.org/ojs/index.php/ejssm/article/viewArticle/75>.]
- , and Coauthors, 2012a: The pretornadic phase of the Goshen County, Wyoming, supercell of 5 June 2009 intercepted by VORTEX2. Part I: Evolution of kinematic and surface thermodynamic fields. *Mon. Wea. Rev.*, **140**, 2887–2915.
- , and Coauthors, 2012b: The pretornadic phase of the Goshen County, Wyoming, supercell of 5 June 2009 intercepted by VORTEX2. Part II: Intensification of low-level rotation. *Mon. Wea. Rev.*, **140**, 2916–2938.
- Marquis, J., Y. Richardson, P. M. Markowski, D. Dowell, and J. Wurman, 2012: Tornado maintenance investigated with high-resolution dual-Doppler and EnKF analysis. *Mon. Wea. Rev.*, **140**, 3–27.
- Mashiko, W., H. Niino, and K. Teruyuki, 2009: Numerical simulations of tornadogenesis in an outer-rainband minisupercell of Typhoon Shanshan on 17 September 2006. *Mon. Wea. Rev.*, **137**, 4238–4260.
- Noilhan, J., and S. Planton, 1989: A simple parameterization of land surface processes for meteorological models. *Mon. Wea. Rev.*, **117**, 536–549.
- Potvin, C. K., A. Shapiro, T.-Y. Yu, J. Gao, and M. Xue, 2009: Using a low-order model to detect and characterize tornadoes in multiple-Doppler radar data. *Mon. Wea. Rev.*, **137**, 1230–1249.
- Rasmussen, E. N., J. M. Straka, R. Davies-Jones, C. A. Doswell III, F. H. Carr, M. D. Eilts, and D. R. MacGorman, 1994: The Verifications of the Origins of Rotation in Tornadoes Experiment: VORTEX. *Bull. Amer. Meteor. Soc.*, **75**, 995–1006.
- Romine, G. S., D. W. Burgess, and R. B. Wilhelmson, 2008: A dual-polarization-radar-based assessment of the 8 May 2003 Oklahoma City area tornadic supercell. *Mon. Wea. Rev.*, **136**, 2849–2870.
- Rotunno, R., 2013: The fluid dynamics of tornadoes. *Annu. Rev. Fluid Mech.*, **45**, 59–84.
- , and J. B. Klemp, 1985: On the rotation and propagation of simulated supercell thunderstorms. *J. Atmos. Sci.*, **42**, 271–292.
- Ryzhkov, A. V., T. J. Schuur, D. W. Burgess, and D. S. Zrnic, 2005: Polarimetric tornado detection. *J. Appl. Meteor.*, **44**, 557–570.
- Schenkman, A. D., M. Xue, and A. Shapiro, 2012: Tornadogenesis in a simulated mesovortex within a mesoscale convective system. *J. Atmos. Sci.*, **69**, 3372–3390.
- Schlesinger, R. E., 1978: A three-dimensional numerical model of an isolated thunderstorm. Part I: Comparative experiments for variable ambient wind shear. *J. Atmos. Sci.*, **35**, 690–713.
- , 1980: A three-dimensional numerical model of an isolated thunderstorm. Part II: Dynamics of updraft splitting and mesovortex coupled evolution. *J. Atmos. Sci.*, **37**, 395–420.
- Shabbot, C. J., and P. M. Markowski, 2006: Surface in situ observations within the outflow of forward-flank downdrafts of supercell thunderstorms. *Mon. Wea. Rev.*, **134**, 1422–1441.
- Shapiro, A., K. M. Willingham, and C. K. Potvin, 2010: Spatially variable advection correction of radar data. Part II: Test results. *J. Atmos. Sci.*, **67**, 3457–3470.
- Snook, N., and M. Xue, 2008: Effects of microphysical drop size distribution on tornadogenesis in supercell thunderstorms. *Geophys. Res. Lett.*, **35**, L24803, doi:10.1029/2008GL035866.
- Straka, J. M., E. N. Rasmussen, R. P. Davies-Jones, and P. M. Markowski, 2007: An observational and idealized numerical examination of low-level counter-rotating vortices in the rear flank of supercells. *Electron. J. Severe Storms Meteor.*, **2** (8). [Available online at <http://www.ejssm.org/ojs/index.php/ejssm/article/viewArticle/32>.]
- Trapp, R. J., 1999: Observations of nontornadic low-level mesocyclones and attendant tornadogenesis failure during VORTEX. *Mon. Wea. Rev.*, **127**, 1693–1705.
- , G. J. Stumpf, and K. L. Manross, 2005: A reassessment of the percentage of tornadic mesocyclones. *Wea. Forecasting*, **20**, 680–687.
- Wakimoto, R. M., and N. T. Atkins, 1996: Observations of the origins of rotation: The Newcastle tornado during VORTEX 94. *Mon. Wea. Rev.*, **124**, 384–407.
- , and H. Cai, 2000: Analysis of a nontornadic storm during VORTEX 95. *Mon. Wea. Rev.*, **128**, 565–592.
- Wang, Y., T.-Y. Yu, M. Yeary, A. Shapiro, S. Nemati, M. Foster, D. L. J. Andra, and M. Jain, 2008: Tornado detection using a neuro-fuzzy system to integrate shear and spectral signatures. *J. Atmos. Oceanic Technol.*, **25**, 1136–1148.
- Wicker, L. J., and R. B. Wilhelmson, 1995: Simulation and analysis of tornado development and decay within a three-dimensional supercell thunderstorm. *J. Atmos. Sci.*, **52**, 2675–2703.
- Wilhelmson, R. B., and J. B. Klemp, 1978: A numerical study of storm splitting that leads to long-lived storms. *J. Atmos. Sci.*, **35**, 1975–1986.
- Wurman, J., D. Dowell, Y. Richardson, P. Markowski, E. Rasmussen, D. Burgess, L. Wicker, and H. B. Bluestein, 2012: The second Verification of the Origins of Rotation in Tornadoes Experiment: VORTEX2. *Bull. Amer. Meteor. Soc.*, **93**, 1147–1170.
- Xue, M., K. K. Droegemeier, V. Wong, A. Shapiro, and K. Brewster, 1995: ARPS version 4.0 user's guide. Center for Analysis and Prediction of Storms, 380 pp. [Available online at <http://www.caps.ou.edu/ARPS>.]
- , —, and —, 2000: The Advanced Regional Prediction System (ARPS)—A multi-scale nonhydrostatic atmospheric simulation and prediction model. Part I: Model dynamics and verification. *Meteor. Atmos. Phys.*, **75**, 161–193.
- , and Coauthors, 2001: The Advanced Regional Prediction System (ARPS)—A multi-scale nonhydrostatic atmospheric simulation and prediction model. Part II: Model physics and applications. *Meteor. Atmos. Phys.*, **76**, 143–166.
- , D.-H. Wang, J.-D. Gao, K. Brewster, and K. K. Droegemeier, 2003: The Advanced Regional Prediction System (ARPS), storm-scale numerical weather prediction and data assimilation. *Meteor. Atmos. Phys.*, **82**, 139–170.
- , M. Hu, and A. Schenkman, 2013: Numerical prediction of 8 May 2003 Oklahoma City tornadic supercell and embedded tornado using ARPS with the assimilation of WSR-88D data. *Wea. Forecasting*, in press.